4-2016

Reverberation Mapping of the Dusty Torus in Active Galactic Nuclei

Erich Franz Geisert

Reverberation Mapping of the Dusty Torus in Active Galactic Nuclei

by

Erich Franz Geisert

Bachelor of Science
Astronomy and Astrophysics
Florida Institute of Technology
2011

A thesis
submitted to the College of Sciences at
Florida Institute of Technology
in partial fulfillment of the requirements
for the degree of

Master of Science
in
Space Sciences

Melbourne, Florida
April 2016

We the undersigned committee hereby recommend
that the attached document be accepted as fulfilling in
part the requirements for the degree of
Master of Science in Space Sciences.

"Reverberation Mapping of the Dusty Torus in Active Galactic Nuclei",
a thesis by Erich Franz Geisert

Daniel Batcheldor, Ph.D.
Associate Professor, Physics and Space Sciences
Major Advisor

Eric Perlman, Ph.D.
Professor, Physics and Space Sciences
Committee Member

Véronique Petit, Ph.D.
Assistant Professor, Physics and Space Sciences
Committee Member

Isaac Silver, Ph.D.
Assistant Professor, College of Aeronautics
External Committee Member

Daniel Batcheldor, Ph.D.
Interim Department Head, Physics and Space Sciences

Abstract

TITLE:	Reverberation Mapping of the Dusty Torus in Active Galactic Nuclei
AUTHOR:	Erich Franz Geisert
MAJOR ADVISOR:	Daniel Batcheldor, Ph.D.

The Dusty Torus is a structure that is believed to exist in Active Galactic Nuclei. The Torus is physically too small to be spatially resolved, so Reverberation Mapping can be performed in order to replace spatial resolution with temporal resolution, yielding observations that can unravel the mystery of the Dusty Torus. One of the unknowns about the Torus is how the dust is distributed. The two competing theories are that either the dust resides in discrete clouds or that there is a solid wall of dust. This thesis presents the results of a year long observation program, starting in August 2011, that surveyed 12 Active Galactic Nuclei. Their fluxes were measured in two wavelengths: 3.6 and 4.5 μm. These two light curves were cross correlated with each other in a process called Flux Redistribution/Random Subset Selection in order to measure the lag in the signal between them. If there are discrete clouds of dust, the interchannel lag should be much smaller than the lag between the continuum and the 3.6 μm emissions. If there is a solid wall of dust, then the lag should be either as long or longer than the lag behind the continuum. Only one of the Active Galactic Nuclei, NGC 6418, had a measurable time lag, which was $12.3^{+2.3}_{-1.9}$ days. This result, paired with estimates of the lag between the AGN continuum and the 3.6 μm emissions, is consistent with the discrete clouds theory.

Contents

List of Figures

List of Tables

List of Symbols, Nomenclature or Abbreviations

AGN	**A**ctive **G**alactic **N**uclei
DT	**D**usty **T**orus
EM	**E**lectro**m**agnetic
FR/RSS	**F**lux **R**andomization/**R**andom **S**ubset **S**election
FWHM	**F**ull **W**idth at **H**alf **M**aximum
IRAC	**I**nfra**r**ed **A**rray **C**amera
MJD	**M**odified **J**ulian **D**ate
MOPEX	**Mo**saicker and **P**oint Source **Ex**tractor
NIR	**N**ear **I**nfrared **R**adiation
PSF	**P**oint **S**pread **F**unction
QSG	**Q**uasi-**S**tellar **G**alaxy
QSO	**Q**uasi-**S**tellar **O**bject
RL	**R**adio-**L**oud galaxy
RQ	**R**adio-**Q**uiet galaxy
SMBH	**S**uper**m**assive **B**lack **H**ole
SNR	**S**ignal to **N**oise **R**atio
SST	**S**pitzer **S**pace **T**elescope
WFPC2	**W**ide **F**ield and **P**lanetary **C**amera 2

Acknowledgements

I wish to say thank you to my family and friends who have kept me going during my graduate studies. My parents, Steve and Margaret Geisert, and my brother, Steven Geisert, have supported my academic goals and will hopefully continue to support me in my post-academic goals as well. Between my friends I made in high school and the friends I have made in my tenure at Florida Institute of Technology, their support has helped me overcome the obstacles that stood in my way. Also, I wish to say thanks to the people in the 3rd Floor Astro Lab, especially Trisha Doyle, for putting up with the gratuitous questions I had for them. Thank you to Rebeca Kinser for her love and support.

I want to say thanks to Dr. Daniel Batcheldor for giving me continued advice throughout my postgraduate studies and for also making me find the answers to questions I had. It helped me gain a better understanding for whatever I had originally asked. I also wish to say thanks to my committee members.

This work is based [in part] on observations made with the Spitzer Space Telescope, which is operated by the Jet Propulsion Laboratory, California Institute of Technology under a contract with NASA.

Dedication

I dedicate this to my Grandparents and my Aunt Erika. I miss them all, and wish they could've been here to see this.

Chapter 1

Introduction

1.1 General Background

Active galactic nuclei (AGN) have been studied by astrophysicists for almost 100 years, and yet new information about them continues to pour in. The first real hint of AGNs came from Slipher (1917). He used data on NGC 1068, taken in 1913 from the Lowell Observatory, to measure emission lines. He found that NGC 1068 had a mean radial velocity of $\sim$ 1120 km s^{-1}. He also noted that the spectra showed that the emission lines did not produce images of the slit, as they usually did, but rather "disks." Slipher went on to reject the broadened slit images, which meant the emissions were spread over large portions of the electromagnetic (EM) spectrum as being formed by extreme radial velocities. AGN research was slow until two separate events in the Astrophysics community: Carl Seyfert's seminal paper (Seyfert, 1943) and the birth of radio astronomy.

The first "real" paper on the subject of radio astronomy, Jansky (1932),

measured three types of radio static, two of which were attributed to terrestrial thunderstorms. The third type of static, which was weak and constant, seemed to change direction over the course of the day. Jansky attributed this static to the Sun. The static was then later corrected to emanate from a fixed point in space that seemed to coincide with the center of the Milky Way Galaxy (Jansky, 1933). Further data would later definitely constrain the largest source of radio static to be the center of the Milky Way (Jansky, 1935). Jansky did notice that the radio static was present when looking at the Milky Way disk, but at levels that were less than the radio static coming from center.

NGC 1068 was once again examined and was found to have emission lines that had a radial velocity of ~ 3000 km s^{-1} (Seyfert, 1943) This was different than Slipher's result, because Seyfert measured the doppler velocity. Higher velocities were found in NGC 3516 and NGC 7469 as well. The full impact of Seyfert (1943) will be covered more in depth in Section 1.4. Astrophysicists spent the next years mostly cataloging AGN. Finally, the groundwork on AGN as a whole was laid down by Greenstein and Schmidt (1964). Greenstein and Schmidt determined that the high redshifts of AGN, specifically 3C 48 and 3C 273 in their paper, were caused by cosmological redshifts. Using the redshifts, they determined that the galaxies were at a distance not less than about 400 Mpc (they did use the now incorrect value for $H_0 = 100$ km s^{-1} Mpc^{-1}). The AGN used by Greenstein and Schmidt (1964) were quasars, or quasistellar objects (QSOs), which were thought to be entirely different objects from Seyfert galaxies. QSOs appeared to observers to be exceptionally bright point sources, especially in the radio portion of the EM spectrum, while Seyfert galaxies had resolvable host galaxies.

Shortly after Greenstein's discovery, an additional class of objects called quasistellar galaxies (QSGs) was discovered (Sandage, 1965). These QSGs were point sources like QSOs, except that they did not have any where near the same radio luminosities as QSOs. In addition, Sandage also found that at brighter magnitudes, the category of QSGs is dominated by objects that are close to the color of stellar objects, whereas at the dimmer magnitudes, the category is dominated by bluer objects, called "interlopers" and "blue stellar objects," which also makes these objects incredibly similar to quasistellar radio sources. On top of that, Sandage also determined that the bluer objects did not match normal extragalactic predictions for the expected photon counts for objects at the distance they are being observed. His answer to this dilemma was that the bluer galaxies matched predictions made for a group of objects that are all at high redshift.

When the spectra of QSOs were analyzed further, they were found to contain chemical abundances similar to the Milky Way. Because the Milky Way is considered a typical galaxy, in that it has old stars and isn't active, this led astrophysicists to believe that QSOs are younger galaxies and that galaxies achieve their chemical compositions early in their life. This led astrophysicists to believe that the objects were relatively short lived, as they had attained their chemical compositions early in the universe's existence. This is further corroborated by Boyle et al. (2002), as they showed that the number density of AGN peak at a redshift of $\sim$z = 2 to 3, which corresponds to the universe being 2 to 3 billion years old, showing that AGN formed early in the universe's history, but seemed to "switch off" and become normal galaxies. In addition to this, QSOs were found to have many different absorption lines spread over many wavelengths,

which happened to be found on the shorter side of the QSO's Lyman-α emission line. This phenomenon was first noticed in 4C 05.34's spectrum. Lynds (1971) hypothesized that the absorption lines were all from the Lyman-α transition, only at different redshifts. This later became known as the "Lyman-α forest," which is an important tool to astrophysicists today, as it allows us to map the intergalactic medium.

Around the same time, Salpeter (1964) posited that the high luminosities of QSOs comes from the idea that there exists an incredibly massive object, at the center of the QSO, which has gas orbiting it in an accretion disk. The massive object was found to probably be a collapsed mass, which is another term for a black hole, of $10^7 - 10^9$ $M_\odot$ (Lynden-Bell, 1969). Additionally, Lynden-Bell also using cosmological arguments to determine that the average distance between old, dead quasars would be ≈ 3 Mpc, which is enough to suggest that most, if not all, galaxies could have been a quasar at some point in time. The mechanism that was used to explain the luminosities observed was that the accretion disk particles eventually begin to spiral into the collapsed object due to turbulent interactions that remove angular momentum. The energies released by this process were predicted to be high enough to create the luminosities seen. A rough estimate of the energy that is released when a particle falls onto the black hole is shown:

$$
\begin{aligned}
\mathrm{E} &= \frac{1}{2} * U \\
&= \frac{1}{2} * -\frac{GM_{\mathrm{BH}}m}{R} \\
&= \frac{1}{2} * -\frac{GM_{\mathrm{BH}}m}{R_{\mathrm{inf}}} - \left(-\frac{GM_{\mathrm{BH}}m}{R_{\mathrm{s}}}\right) \\
&= \frac{1}{2} * \left(0 + \left(\frac{GM_{\mathrm{BH}}m}{R_{\mathrm{s}}}\right)\right) \\
&= \frac{1}{2} * \frac{GM_{\mathrm{BH}}m}{\frac{2GM_{\mathrm{BH}}}{c^2}} \\
&= \frac{1}{4}mc^2
\end{aligned}
$$

Where E is the total energy of the system, U is the gravitational potential energy, G is the gravitational constant, M_{BH} is the mass of a black hole, m is the mass of a particle, $R_{\mathrm{s}} = \frac{2GM_{\mathrm{BH}}}{c^2}$ is the Schwarzchild radius of a black hole, and c^2 is the speed of light squared. Using the virial theorem, where $E_{\mathrm{tot}} = \frac{U}{2}$, the maximum energy that can be released from a particle infalling onto a black hole is $\frac{1}{4}$ the energy of its rest mass. If the derivative of the energy released, with respect to time, is taken:

$$
\begin{aligned}
\frac{dE}{dt} &= \frac{d(1/4mc^2)}{dt} \\
&= \frac{1}{4}c^2 * \frac{dm}{dt} \\
&= \frac{1}{4}\dot{m}c^2
\end{aligned}
$$

where $\dot{m}$ is the mass accretion rate of the black hole, then the end result is the maximum luminosity that could be generated by matter accreting onto a

black hole. This maximum luminosity assumes perfect efficiency.

Salpeter also noted that this process is inefficient in more evolved galaxies, such as the Milky Way, because the dust particles actually inhibit the process, making the luminosity that is generated too low while also making the process go slower, which makes it take longer than expected. This leads itself to the idea that most, if not all, of these QSOs are young galaxies, filled with stars of low metallicity, compared to older galaxies which have stars of high metallicity. Salpeter's idea would later be taken to be part of the Standard Model for AGN.

1.2 AGN Emissions

AGN have an array of different observational characteristics. Because of the differences, over the years, AGN were split into many different classifications. Until recently, each class of object was thought to be entirely separate from each other. But, observational evidence has shown that the different types of objects are not in fact wholly different objects, but rather all part of the same phenomenon. The observational characteristics come from the fact that AGN have a high luminosity across a wide portion of the EM spectrum, ranging from the Radio portion to the X-ray portion. The overall emission from the AGN comes from multiple different mechanisms.

The major features of the spectra (Figure 1.1) are the IR Bump, Big Blue Bump, the soft x-ray excess, and the reflection component. Additionally, Radio-loud galaxies (RL) will also contain a strong radio emission. Seyfert galaxies also contain a feature in the X-ray spectrum called the FeKα line. The FeKα is a florescence emission line caused by the reprocessing of the X-ray emissions

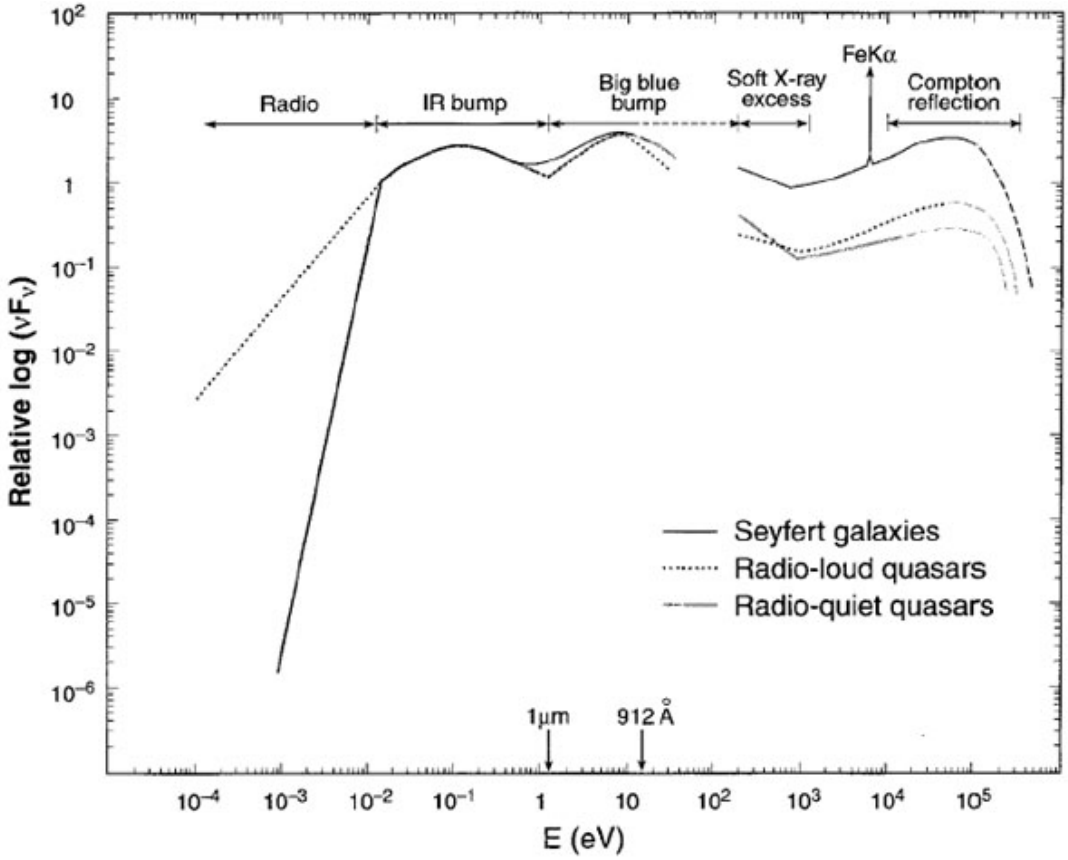

Figure 1.1: A sample spectrum from a typical AGN (Koratkar and Blaes, 1999). The missing data at $\sim$ 100eV arises, in part, from self-absorption.

in the AGN itself.

The mechanism for the emission of the UV, blue, and green light has been determined to come from an accretion disk that orbits the supermassive black hole (SMBH) at the center of the AGN. As the material of the disk orbits the SMBH, the accretion disk undergoes collisional heating, with the inner disk heating up to a higher temperature than the outer part of the disk, leading to a thermal gradient, due to the increasing orbital velocity at radii closer to the SMBH. All of the particles, at a given radius, would therefore have the same temperature, and thus would radiate the same energy as blackbodies. Each radius emits as a blackbody at different temperatures, which, when taken over the entire disk, sum to a continuum of light, ranging from the UV to roughly green part of the spectrum. This continuum is referred to as the Big Blue Bump (BBB) (Kazanas et al., 2012). This BBB provides a large portion of the luminosity found in AGN. The BBB is considered the engine of an AGN because it is theorized to power most of the other emission processes in AGN.

The mechanism for the radio emissions comes from synchrotron radiation, specifically found within relativistic jets that are being launched by the AGN. Synchrotron radiation occurs when relativistic electrons spiral along magnetic field lines. Accelerating charges emit photons, thus charges that are spiraling are under a constant acceleration and therefore continuously emit photons. While the actual source of AGN jets is not completely known, what is known is that the jets from AGN are moving at relativistic speeds, and that the jets will contain charged particles. The relativistic velocity of the jet material has been seen in what astrophysicists call superluminal motion. From observations, the jets appear to move at apparent speeds that exceed the speed of light. This

phenomenon was later found to be an optical illusion that arises when the jet is both moving at relativistic speeds and is emitting photons at close to the observer's line of sight (Rees, 1966). Synchrotron radiation is almost identical to cyclotron radiation, with the key difference being that cyclotron radiation is emitted from electrons that are not moving at relativistic speeds.

The infrared emission mechanism is thought to come from thermal emissions of a large torus of material called the Dusty Torus. This will be further expounded upon in Section 1.4.1.

X-ray radiation can be found in most AGN. But, significantly more X-ray emissions are found in radio-loud AGN (discussed in 1.3). The mechanism for the X-ray emissions comes from Inverse Compton scattering. Compton Scattering is the process by which an energetic photon scatters off an electron. The scattering transfers energy from the photon, increasing its wavelength, to the electron, increasing its velocity. Inverse Compton scattering is the reverse process, whereby a relativistic electron scatters a low energy photon, transferring energy to the photon, which shortens the wavelength. The low energy photons are believed to originate from within the accretion disk, via thermal emission. They will travel above the plane of the disk and encounter relativistic electrons found within a corona around the accretion disk and also within relativistic jets, if they are present. The relativistic electrons will scatter the low energy photons and produce X-ray emissions from both sources. This explains why AGN both with and without jets can have X-ray emissions.

In addition to the continuum emission mechanisms, AGN also have multiple mechanisms for the spectral line emissions as well. The two most notable sets of line emissions are the Broad-line emissions and the Narrow-line emissions.

Optical emissions, from the accretion disk, are absorbed and re-emitted by gas clouds. The difference between the Broad and Narrow-line emissions comes from two sources: spatial location and emission line mechanisms. This is covered in Section 1.4.

1.3 Unification Theory

QSOs are separated into two overarching classifications: radio-loud (RL) and radio-quiet (RQ) (Antonucci, 1993). The only difference between the two classifications is that the RL QSO have additional radio emissions. But, the UV/Optical/IR emissions of the RLs are similar to those of the RQs. So, the RLs and RQs are believed to be the same fundamental objects, except that there are huge sources of radio emissions from the RLs in addition to the RQ core. There are subclasses of AGN within each classification. For RQ AGN, the difference between the subclasses are based more on orientation and resolvability. When the host galaxy of the AGN is resolved, it is a Seyfert galaxy, which are separated into Types 1 and 2. If the host galaxy is very faint compared to the AGN then it is classified as a quasi-stellar object (QSO). The focus of this thesis is on Seyfert galaxies, so they will be explained more in Section 1.4.

The RL class has more subclasses within it, due to the additional emission sources that are found in RL QSO. The largest distinction in RL QSO is whether the emission source is an extended or compact radio source. For extended radio sources, the emission source is found within lobes that are away from the central galaxy. The Fanaroff-Riley classification (FR) is based on the location of the extended radio emission source in the QSO. FR-I classed RL QSOs have the

emission sources within the central galaxy, while FR-II have the sources found outside of the central galaxy (Fanaroff and Riley, 1974). Observationally, the FR-I QSO have only a single source of radio emission, in the core, while the FR-II QSO have two lobes of radio emission. FR-II AGN typically have their radio lobes found at the end of their jets.

The Figure 1.2 shows a graphical representation of the different classifications of AGN, with half of the diagram showing the RL classifications and the other half showing the RQ classifications.

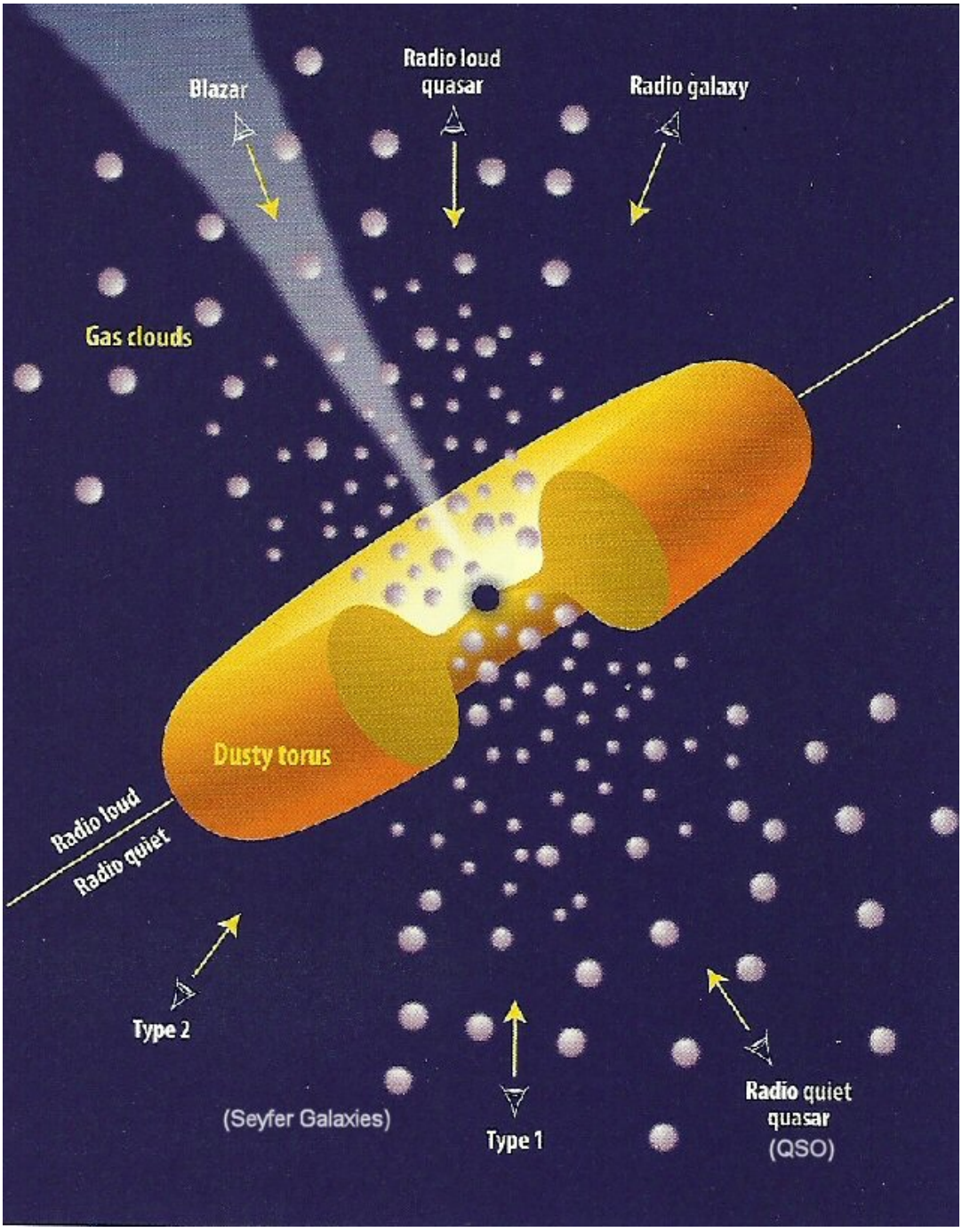

Figure 1.2: A graphic representation of the different classifications of AGN, based on the observer's angle to the AGN. Found at https://universe-review.ca/I05-02-AGN2.jpg, from *Gravity's Fatal Attraction*, by M. Begelman and M. Rees.

1.4 Seyfert Classification

AGN can be separated into an additional two categories; Type 1 and Type 2 (Seyfert, 1943). A Type 1 AGN is an AGN that exhibits both broad line emissions ($\approx 2000 - 5000$ km s^{-1}) and narrow line emissions (≈ 500 km s^{-1}) in its spectrum. A Type 2 AGN only exhibits narrow-line emissions. Both RL and RQ AGN can be either Type 1 or Type 2, but quasars are almost exclusively Type 1. Furthermore, if the host galaxy of an AGN is able to be detected, it is known as a Seyfert galaxy (i.e. an AGN that has the host detectable and is a Type 1 AGN is known as a Seyfert 1, or Sy 1 for short).

The two types of lines come from different regions near the galaxy's core, with the broad-line region (BLR) being closer to the accretion disk and the narrow-line region (NLR) being further away from the accretion disk. The width of the lines, that are emitted by either region, is a direct result of Doppler broadening: the BLR orbits closer to the SMBH than the NLR does. The large gravitational well of the SMBH causes clouds of gas that are deeper into the potential to orbit with a larger velocity. So, the BLR has a larger orbital velocity, due to being deeper in the well, which in turn causes the line emissions to be more broad than the line emissions from the NLR. Typically, the kind of Doppler broadening that is seen in emission lines is Thermal Doppler Broadening, which is when the thermal motions of a particle cause the emitted photon to have a shifted wavelength of light than it would have if it was at rest. Thermal Doppler Broadening follows a Gaussian line profile with a full-width half maximum (FWHM) of

$$(\delta\lambda)_{1/2} = \frac{2\lambda_0}{c}\sqrt{\frac{2k_BT}{m}\ln(2)}$$

where $\delta\lambda$ is the shifted wavelength, λ_0 is the rest wavelength, k_B is the Boltzmann constant, T is the temperature of the gas that is emitting, and m is the mass of the particle. For the BLR, Thermal Doppler Broadening can not be the dominant source of broadening of the emission lines, because of the measured velocities. For a velocity of $\sim$ 5000km s^{-1}, the temperature would have to be $T \sim 10^9$K, which is a high enough temperature to completely ionize all of the atoms in the BLR. So, Doppler Broadening must have some bulk motion involved, which makes the FWHM of the emission line profile

$$(\delta\lambda)_{1/2} = \frac{2\lambda_0}{c}\sqrt{\left(\frac{2k_BT}{m} + v^2\right)\ln(2)}$$

with v as a bulk velocity. If the assumption that both the temperature term and the bulk velocity term contribute equally to the overall observed velocity is made, then the temperature of the gas would be $\sim 10^7$K, which is still too hot for emission processes. So, the dominant factor in the broadening of the BLR emission lines is the radial velocity of the gas as it orbits the SMBH. At the temperatures typically seen in the BLR ($\sim 10^4$K), the contribution from the thermal effects are about three orders of magnitude smaller than the contribution from the orbital motion would be, so the assumption that the BLR emissions are broadened almost exclusively by the doppler motions of the gas itself can be made.

In addition to the radius at which the emitting regions are located, the types of lines that are detected are different between the two, with the BLR having

permitted emission lines and the NLR having forbidden emission lines. Most permitted emission lines are formed by atoms that have been excited into an energy level (also called an orbital) higher than the ground state. Gas clouds in the BLR will absorb a photon of light (typically from the continuum) which will promote an electron to a higher energy level, sometimes even ionizing the electron in a process called photoionization. In the event of a photoionized electron, the electron will eventually recombine with an ion (aptly called recombination). Most of the time, when the electron recombines it will still be in an excited state, so the electron will eventually spontaneously transition down from one energy level to a lower energy. As it transitions down, it will emit a photon that has the same energy as the difference between the energy states that it is transitioning between. When an electron transitions multiple times, it is called a cascade.

Forbidden emission lines on the other hand, have a similar transition process, but instead of high energy photons photoionizing the particles, the particles themselves undergo collisional excitation, where the particles collide and gain energy. Instead of promoting the electron to higher orbitals, the particle is promoted to a meta-stable state, which persists much longer than the energy states associated with photoionization. The particle eventually spontaneously transititons to a lower energy state and emits a photon at a specific wavelength. Forbidden emission lines are not actually forbidden by the laws of physics from happening, but instead are called forbidden because they can not be observed on Earth. Forbidden emission lines require a very low density of particles be observed, because otherwise the higher energy particles will collide with other particles and undergo the reverse process, called collisional de-excitation. So

far, forbidden lines have only been seen in the spectra of gas clouds in space, as the clouds can achieve the very low densities needed.

The fact that forbidden lines are seen in the NLR means that the NLR must have a very low density, while the fact that the BLR contains no forbidden lines means that the BLR must have a high density. If both forbidden and permitted lines are able to be seen, in roughly equal luminosities, then the density of the gas is at the forbidden lines' critical density, or that the two spatial components are superimposed. The critical density is the where the emission from forbidden processes is equal to the emission of the permitted processes. Once the density of a gas surpasses the critical density of a forbidden mechanism, the forbidden line becomes rapidly quenched and the only emission mechanism that can be observed is the permitted emission mechanism. For the NLR, the more likely scenario is that some clouds in the NLR will emit via the permitted mechanism and some will emit via forbidden mechanisms.

1.4.1 Dusty Torus

The dusty torus (DT) is the cornerstone of the Unification Theory for Seyfert 1 and 2s. The idea of the standard model is that Type 1 and 2 AGN are fundamentally the same objects, but only appear different due to the orientation, much like how a galaxy that appears to be thin dust disk when viewed edge-on turns out to be a grand design spiral when viewed face-on. The DT is thought to exist between the BLR and NLR of an AGN (Antonucci and Miller, 1985). Figure 1.2 shows this phenomenon: In the RQ portion of the diagram, the Type 1s are seen when the angle between the AGN and the observer is large enough that the DT doesn't impede the BLR emissions from being observed, while the

Type 2s are seen when the angle is small enough that the DT is blocking the BLR emissions from being observed. The gas clouds in the figure generally represent the two different emission regions, where the smaller clouds, signifying the BLR, are closer to the SMBH and are only seen if the DT is not blocking their emissions.

Summary

AGNs are some of the most powerful objects in the universe, capable of emitting large amounts of EM radiation throughout the entire spectrum, which is a feat that is not matched by any other object. The driving force behind AGN is an SMBH that has an accretion disk feeding it matter. The disk emits as a summation of blackbodies to form an ultraviolet/blue continuum of radiation (BBB). This continuum serves to directly power the infrared emissions while also indirectly powering the X-ray emissions of the AGN. In a large portion of AGN, there exists a large radio-emission component in the spectrum, which, in addition to providing the radio emissions for the AGN, also contributes to the X-ray emissions of the AGN. Other parts of the X-ray emissions stem from reflections and fluorescence on the accretion disk. AGN themselves are classified into different categories, with the idea that the different categories are derived almost solely from the observation angles of AGN. AGN that both are radio-quiet and reside in resolvable host galaxies are the Seyfert galaxies, and will either be Type 1 or 2 galaxies, depending on whether broad and narrow emission lines are found (Type 1), or if only narrow emission lines are found (Type 2). The difference between the two is theorized as a large torus of dust, and that

the angle of the galaxy with respect to an observer is what will actually make the classification, with the torus either obscuring the broad line regions (Type 2) or not obscuring the broad line regions (Type 1). Table 1.1 contains a brief summary of the major classifications of AGN.

One of the key aspects of the DT that is unknown is the actual size of the torus. It must lie farther from the accretion disk than the BLR, otherwise the obscuring theory would not make sense. Additionally, the structure of the DT is unknown. The two competing theories are that either the DT is a large ensemble of clouds of dust, with space between each cloud, or that the DT is composed of a near-solid wall of dust. This thesis aims to study the structure of the DT, while also constraining its spatial size and matter distribution.

Table 1.1: Observational properties of the different classifications of AGN. [(1)] Seyfert galaxies can be either RL or RQ, but an overwhelming majority of Seyfert galaxies are RQ.

Classification	Radio	Infrared	Ultraviolet/Blue Continuum	Emission Lines **Broad**	**Narrow**	X-Ray
			Radio Loud			
Type 1 Radio Galaxy	Yes	Yes	Yes	Yes	Yes	Some
Type 2 Radio Galaxy	Yes	Yes	Somewhat	No	Yes	Some
Quasar	Very strong	Yes	Yes	Yes	Yes	Very Strong
			Radio Quiet			
Seyfert[1] 1	Little	Yes	Yes	Yes	Yes	Little
Seyfert 2	Little	Yes	Somewhat	No	Yes	A little

Chapter 2

Reverberation Mapping

2.1 Classical Reverberation Mapping

"Classical" Reverberation Mapping is a technique that can be used to reconstruct otherwise spatially unresolved structures in a target by monitoring the delay in optical variation of the continuum and emission lines of an AGN; its variations can be used to detect the response of the region that is being mapped. Originally, reverberation mapping was developed in order to map the BLR of Seyfert AGN (Peterson and Horne, 2004). The basic idea behind reverberation mapping is relatively simple. What happens in an AGN is that the continuum supplies the radiation that "powers" the BLR. The BLR absorbs and re-emits the light that the continuum radiates. If a change happens in the continuum, such as a large clump of matter is accreted onto the SMBH, than the change in the light emitted (in this case, more energy would be released) would propagate and accordingly increase the emission line strength in the BLR. Due to the vast distance between the central power source and the BLR, this process is not

instantaneous. So, when a change happens to the central power source, there is a lag until the radiation encounters the BLR. Reverberation mapping of the BLR allows us to place an upper limit on the size of the emission region. Using the radius of the BLR, along with the velocity of the emission clouds, we can use the virial theorem to determine the mass of the SMBH

$$M_{\bullet} = f * \frac{v^2 * R}{G} \tag{2.1}$$

where v is the Doppler broadened velocity of the emission clouds, R is the radius of the emission region, G is the gravitational constant, and f is some geometric covering factor to account for the fact that the geometry of the BLR is not known.

Reverberation mapping relies on a few assumptions. The first is that the continuum, which drives the changes in the BLR, is emitted from a single, central source. For AGN, this assumption is likely good, as the continuum originates in the accretion disk, which is a relatively compact region. Astrophysicists know that the continuum is what is driving the change in the BLR emissions, because the BLR emission lines are emission lines formed from ionizing radiation found at the wavelengths of the continuum. Some of the most useful emission lines are the H-α and the H-β lines. The reason for this is that they are readily identifiable and are permitted lines. They are the first two emission lines that are found in the Balmer series for Hydrogen emissions: H-α being the transition from the n = 3 to the n = 2 energy state and H-β being the transition from the n = 4 to the n = 2 energy state, where n = 1 is the ground state for the hydrogen atom (all of the Balmer emission lines involve the electron transitioning

to the n = 2 state). The photoionizing radiation for the BLR comes from the continuum emission, as the BLR is further from the AGN than the accretion disk. Once the hydrogen is photoionized, the electrons will recombine and then begin to cascade down from the higher energy levels to the lower energy levels. Whenever the H-α transition occurs, a photon of 656.3 nm is emitted by the electron.

Another example of an emission line series is the Lyman series, mentioned in Section 1.1. The Lyman series occurs when an electron falls to the first energy level, also called the ground state. Because of the energy gap between even the first and second energy level, the longest wavelength of an emitted photon in the Lyman series is 121.6 nm, which is in the ultraviolet portion of the spectrum.

The second assumption is that the dominating time scale for BLR is the light travel time, or

$$\tau_{\rm LT} = \frac{r}{c} \tag{2.2}$$

where r is the distance from the continuum source to the BLR and c is the speed of light. The ion recombination time scale, which is the length of time necessary for the ions that are photoionized by the continuum source to recombine and re-establish equilibrium, must not be the dominating time scale. For typical Seyfert galaxies, the recombination time scale ($t = (n_e \alpha_{\rm B})^{-1}$) is approximately 6 minutes for typical BLR electron densities $n_{\rm e} \sim 10^{10}$ cm^{-3}, with $\alpha_{\rm B} \approx 2.6 \times 10^{-13}$ cm^3 s^{-1}, the case B recombination rate for hydrogen (Peterson and Horne, 2004).

For mapping the BLR, the basic equation, known as the transfer equation

$$L_i(v,t) = \int_{-\infty}^{\infty} L_c(t')\Psi(v, t-t') \tag{2.3}$$

is used to determine the velocity-delay map of the AGN, where L_i is the line emission luminosity, L_c is the continuum luminosity, v is the Doppler shift, t is the observer time, t' is the time when the continuum signal was emitted, and $\Psi(v, t-t')$ is the velocity-delay map (Blandford and McKee, 1982).

One of the features of reverberation mapping is that the velocity-delay map must also take into account the fact that the continuum signal found in the BLR is observed multiple times. The cause of this is due to the assumed symmetry and orientation of the BLR. For the simplest case, a circular Keplerian orbit BLR oriented edge-on towards the observer, the time delay will be $\tau = (1 + \cos\theta)\frac{r}{c}$ (as seen in Figure 2.1). When the continuum emits its signal, the signal will take τ_{LT} to reach a BLR cloud at radius r from the continuum, on the side closest to the observer ($\theta = \pi$ rad). But, for the signal on the opposite side ($\theta = 0$ rad), the reprocessed signal will have a $\tau = \frac{2r}{c}$. So, in order to build an accurate $\Psi(v, t-t')$ map, we must observe the AGN for long periods of time because, for a distance of x light years, the delay is x years. In order for this to be true, the gas in the BLR must both be transparent and isotropic in distribution. These assumptions introduce the geometric factor seen in Equation (2.1) in order to correct the SMBH's mass based on the actual conditions that are inferred from observations.

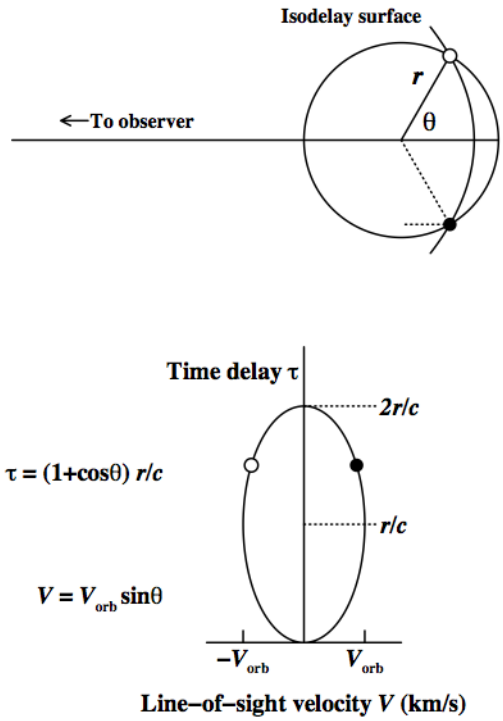

Figure 2.1: This is a visual representation of the best case scenario for a reverberation mapping isodelay surface: circular and oriented edge-on toward the observer (Peterson and Horne, 2004)

.

2.1.1 Continuum Variations

The continuum variations have a wide range of time scales, and likewise physical mechanisms behind them. The different proposed mechanisms range from magnetohydrodynamic instabilities in the accretion disk (disconnection events in the disk) and variable accretion rates to accretion disk reprocessing of X-ray photons from the AGN. Typical timescales seen can range from a week to months, with some AGN varying on a scale of a year. X-ray reprocessing time scales are on the order of tens of seconds, which implies that the X-ray emitter must reside closer to the SMBH than the bulk of the accretion disk; this is typically seen as the gas that emits at the high energy tail of the continuum (Peterson, 2001). Seyfert AGN typically show little variability over a few days.

2.2 Reverberation Mapping the Dusty Torus

This technique can be adapted to mapping the DT, utilizing the fact that the assumptions carry through from the BLR to the DT. For dust emission, the assumption that the dust particles will re-emit absorbed radiation on a time scale significantly smaller than the time scale for the time lag holds. In order to accurately model the DT, the dust composition must be taken into account. According to Mor and Netzer (2012), the torus can be thought to be predominantly composed of two dust grain types: the standard model silicate dust and graphite dust. The two-dust model is significant, because each dust sublimates at a different temperature. The sublimation temperatures are $\sim$1500 K for silicate dust and $\sim$1800 K for graphite dust. An estimate of the inner

edge of the DT can be made using

$$R_{d,C} \simeq 0.5 \left(\frac{L_{\rm bol}}{10^{46}\ {\rm erg\ s^{-1}}} \right)^{1/2} \left(\frac{1800{\rm K}}{\rm T} \right)^{2.8}\ {\rm pc}. \tag{2.4}$$

From (2.4), the radius of a pure graphite torus would be 0.5 pc, about 600 light days. So, the inner radius would have a time lag of about 600 days. But, for the mixed dust model, the equation for the sublimation radius is

$$R_{d,Si} \simeq 1.3 \left(\frac{L_{\rm bol}}{10^{46}\ {\rm erg\ s^{-1}}} \right)^{1/2} \left(\frac{1500{\rm K}}{\rm T} \right)^{2.6}\ {\rm pc}. \tag{2.5}$$

The sublimation radius of a mixed dust torus is 1.3 pc, about 4.2 years. Within 4.2 light years, the mixed dust torus is sublimated out until there is a pure graphite torus. Using these values for the radius of the torus, the expected lag time for a reprocessed signal from the continuum would be, at a minimum, about a year and a half. This is in rough agreement with Raban et al. (2009), as their interferometric results showed that for NGC 1068, the DT starts at around the outer edge of the maser disk, or about 1.1 pc from the center. Using the bolometric luminosity of NGC 1068 to be $L = 5.769$ x 10^{44} ergs per second (Bock et al., 2000), this is well outside the sublimation radius of 0.31 pc, assuming a sublimation temperature of 1500 K for the silicate dust.

2.2.1 Smooth versus Clumpy Torus

In addition to determining the radius from the central source to the DT itself, reverberation mapping can be done across different bandpasses in the infrared wavelengths. This helps to map the physical structure of the torus itself. The

current theoretical models of the structure show that the DT is either a distribution of clumps of dust, a smooth continuous distribution of dust, or a mixture of both, with larger dust clumps within a diffuse, smooth distribution (Stalevski et al., 2013). Observing the delay in reverberation between different bandpasses will allow the structure to be more finely probed, due to the differences in expected behavior for each of the theoretical models. The wavelength emission radius R for a smooth DT is given by

$$R \propto T^{-2.6}$$

where T is the temperature of the emitting dust. Through Wien's Displacement Law ($T \propto \lambda^{-1}$), this means that

$$R \propto \lambda^{2.6}. \tag{2.6}$$

If two wavelengths, x and y, are chosen so that the ratio of their emission radii is some ratio z, then the lag between the continuum and y wavelength should be z times longer than the lag between the continuum and x wavelength, assuming y is a longer wavelength than x. For a clumpy DT, this relation does not hold because the clouds will have a surface brightness profile which will emit over a range of wavelengths. So, for the same wavelengths, the lag between the continuum and wavelengths will much smaller. Additionally, in a clumpy torus, clouds of cooler temperatures can be found much closer to the AGN than should be possible, due to shielding of the cooler clouds by warmer clouds. The clouds that are shielded by the warmer clouds are indirectly heated by clouds around it. Also, clumpy models show that emission from the opposite side of the torus

(on the far side of the AGN) is possible for all orientations of the DT, whereas a smooth profile requires inclination angles of around $\sim 27^{\circ}$ (Nenkova et al., 2008a, and sources within).

Another observable feature that is readily explained by clumpy torus models, unlike smooth models, is the 10 μm feature found in AGN. This feature shows up differently for different AGN classifications. In QSOs, the feature manifests as an emission features. For Seyfert AGN, the feature is either not there or found as a slight absorption feature in Seyfert 1s, while for Seyfert 2s it is a clear absorption feature. Smooth models predict that Seyfert 1 AGN should have this feature as an emission feature and Seyfert 2 AGN should have it as an absorption feature (Nikutta et al., 2009). Clumpy models are able to explain the observed features as consequences of the number and thickness of clumps. Small numbers of clouds along an equatorial ray ($<\sim 5$) will show emission, but a larger number of clouds will show absorption. With the number of clouds predicted to be in any Seyfert AGN equatorial ray (~ 5), emission is almost guaranteed to be very small (Nenkova et al., 2008b). Typically, a clumpy torus will preferentially show absorption features unless the clouds are very thick, or there are numerous clouds. Very bright AGN, on the other hand, tend to have fewer clouds in ray (possibly due to sublimation radius being farther from the AGN) which explains why they show emission.

2.3 Why Use Spitzer?

The sublimation temperatures for the two dust types (1800 K for graphite and 1500 K for silicate) yield a blackbody peak wavelength of 1.6 μm and 1.9

μm, respectively. These fall within the Near-InfraRed (NIR) spectrum, and so only telescopes capable of observing in the NIR can observe these effects. Infrared observations of the AGN should not be taken right at the wavelengths of the sublimating dust, because the dust would not re-emit the photons it was absorbing. Further complications arise from the fact that, due to the AGN variability, the temperature of the dust will vary well, which in turn yields variations in the sublimation radius for the inner edge of the dust. Therefore, a longer wavelength should be used. The K-band (2.2 μm) would be a good candidate for torus observations, except that because the dust that emits at that wavelength is around the temperature of sublimation ($\sim$ 1300 K), it is spatially located near the inner edge of the torus. Dust that is close enough to the inner edge of the torus is subject to grain destruction complications, because if the dust that is sublimated is not replaced by more dust (on a smaller timescale than the variability of the continuum emissions), then the distance from the continuum emission to the torus will be subject to variability, which makes calculating the lag more difficult.

Instead, dust that is farther inside the torus should be sampled. The *Spitzer Space Telescope* (SST) was chosen due to its ability to observe at wavelengths of 3.6 μm and 4.5 μm, where the dust is expected to the reside within the main portion of the torus. This removes the issue of variability in radius. These wavelengths are also good for constraining the dust distribution; from Equation (2.6), the ratio of their radii should be $\frac{R_{4.5}}{R_{3.6}} = \left(\frac{4.5\,\mu\text{m}}{3.6\,\mu\text{m}}\right)^{2.6} \approx 2$, therefore the 4.5 μm lag should be on the order of twice as long as the 3.6 μm lag. The galaxy background at those particular wavelength is also very low, which allows for stronger signals to be obtained from the AGN itself (Axon et al., 2011).

Summary

Constraining the size of structures in AGN is a hard process, because most AGN are far enough away that a majority of the structures can not be spatially resolved. In order to probe the structures such as the BLR or the DT, astrophysicists can replace spatial resolution with temporal resolution with reverberation mapping. Changes in the continuum emission can be tracked in how the BLR and DT respond. But, because the distance between where the continuum is emitted (the accretion disk) and the BLR/DT is large (with the DT being predicted to be on the order of 1 pc in distance), the actual time between when the continuum changes and when the BLR or DT responds is also similarly large. Multiple observations over time allow a velocity-delay map to be built, which can then be used to determine the spatial distance between the SMBH and the structure. In the case of the BLR, the distance can then be used, along with the velocity of the line-emitting gas clouds, to constrain the mass of the SMBH at the center of the AGN. The DT is larger than the BLR, and so the time lags will be much longer. Multiple bandpasses can be used in the reverberation mapping of the DT as well, because each bandpass corresponds to a different radius of dust in the torus. These differences in the delays can be used to obtain more detail on the composition and geometry of the torus, which is what this thesis attempts to do.

Chapter 3

Instrumentation and Data Reduction

3.1 Spitzer Space Telescope

The SST, launched on 2003 August 25, is part of NASA's Great Observatory program. The telescope, and its instruments, were designed to be sensitive in the infrared portion of the electromagnetic spectrum. Specifically, the telescope operates between 3.6 and 160 μm. The telescope itself is split into two main components: the spacecraft and the cryogenic telescope assembly (CTA). The telescope must be kept cool, so the warmer components, such as the power generation plants, telecommunications, avionics, and gyros, are kept separate from the CTA. The reason that the telescope and the scientific instruments must be kept cool is due to the fact that heat from the telescope will introduce more mobile charge carriers into the instruments, called the dark current. Keeping the telescope cold minimizes both these extra mobile charge carriers and the

noise that is introduced through the electronics.

The spacecraft contains a pointing and control system (PCS) and a reaction control system (RCS), both of which have redundant components. The RCS handles the gross movements of the spacecraft, mainly used to unload angular momentum. The RCS utilizes ambient temperature ($\sim$30 K), pressurized nitrogen gas in order to slew the observatory. The PCS contains four reaction wheels, mounted in a pyramid arrangement, gyroscopes, and star trackers. The reaction wheels and gyroscopes work together to ensure that the telescope is precisely pointed, with the star trackers serving as the orientation points for observations.

The CTA contains the telescope, the associated instruments, thermal shields, and a storage container for liquid helium. The telescope itself is composed of a 0.85 m primary mirror and a moveable secondary mirror, which is used to focus the optics. The liquid helium was used in a boil-off configuration, to cool the optics. However, the optics are not cooled directly by the helium boil-off. Instead, the cryostat vacuum shell is directly cooled by the helium, which then leads to the optics being cooled via thermal coupling. Several measures have been taken to help dissipate the solar thermal load on the telescope. The first is a strict adherence to restrictions placed on the hardware that orients the CTA away from direct sunlight. In addition, a high-emissivity black paint has been applied to the side of the CTA that faces away from the Sun. The side of the CTA that faces the thermal shields, solar array, and the spacecraft components is a highly polished aluminum; it reflects the sunlight away from the sensitive CTA. The structure of the CTA is made of beryllium, to minimize thermal expansion and contraction. Figure 3.1 is a representation of the SST at launch.

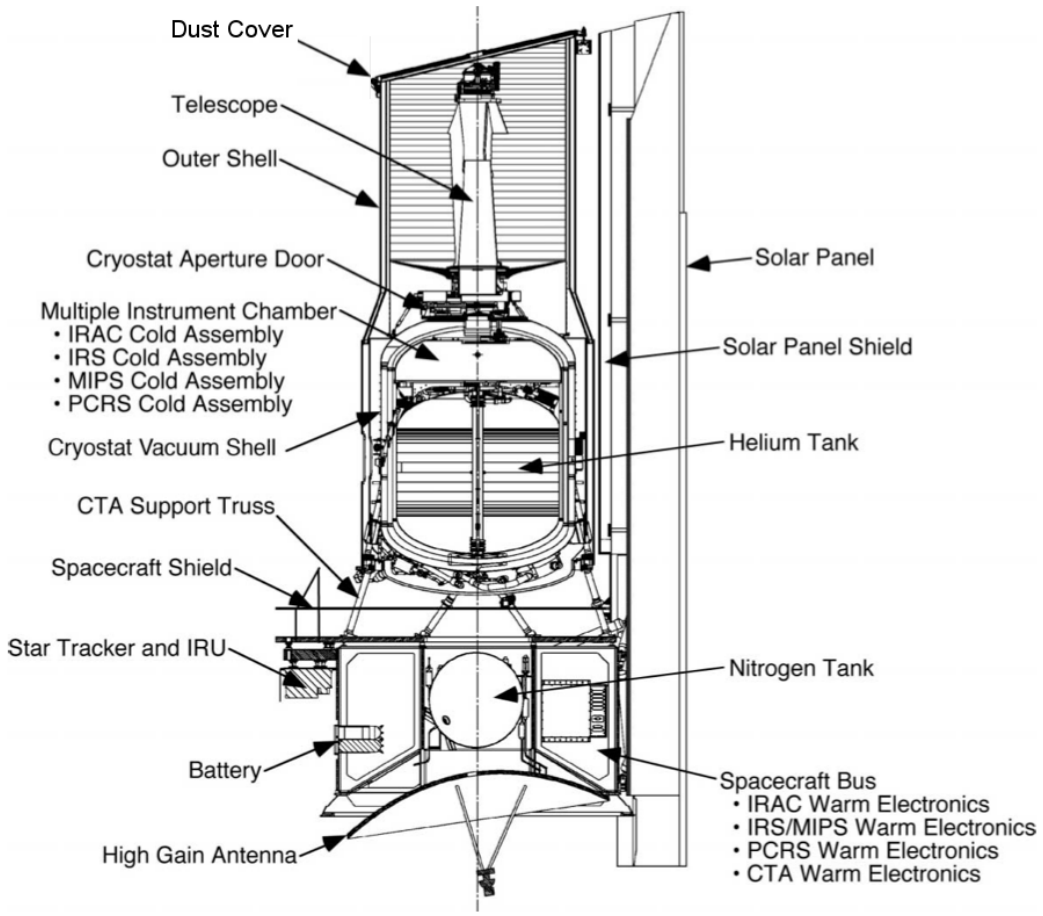

Figure 3.1: A cutaway of the Spitzer Space Telescope, modified from Werner et al. (2004). The modification was including a label of the dust cover, jettisoned after launch, that protected the interior of the telescope.

3.2 IRAC Instrument

The Infrared Array Camera (IRAC) was designed to probe the early universe in large-area, deep surveys. The wavelength range for the instrument is from $3 - 10$ μm, over four different detectors, with each observing in a different bandpass. Channels 1 and 2, which are the channels used by this program, observe in 3.6 μm and 4.5 μm, respectively. The remaining channels, Channel 3 and 4, observe in 5.8 μm and 8.0 μm bandpasses. Each channel observes

simultaneously, with channels 1 and 3 sharing one section of the sky. Channels 2 and 4 observe another section, in a similar setup. Each detector was fitted with a fixed filter, to minimize moving parts and maximize useable space in the instrument. On the IRAC, the only moving part is the shutter at the entrance aperture of the instrument. On 15 May 2009, the cryogen for the SST was depleted, thereby forcing all of the instruments to either function in a "warm mission," or stop functioning (Carey et al., 2010). The IRAC currently operates differently, as it has caveats on its abilities. One of the biggest caveats is that only the two shortest wavelength channels are operable in the warm mission. IRAC also suffers from occasional residual images within each observation. These residuals, known as persistence, almost entirely come from the presence of bright objects within the field of view of the telescope. Typically, taking multiple, short exposures mitigates these residual images. Additionally, the warm mission has affected the electronics slightly. The electronics, for the most part, introduce either positive or negative errors (with the occasional NaN error in pixels as well) in the readout of the images. These are constrained to just the edges of the image. Because all of the AGN in this thesis were the designated targets of the observations, these read errors should not effect the results.

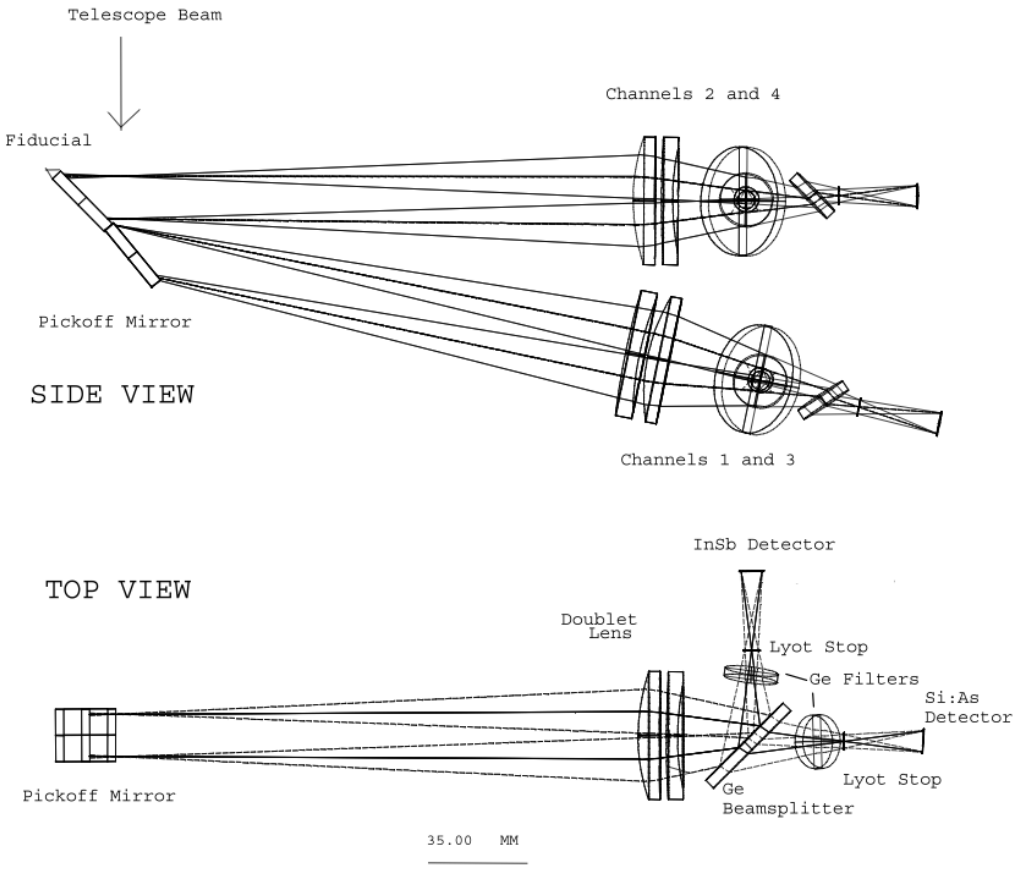

Figure 3.2: The design of the IRAC instrument. Components have been scaled to more adequately show the instrument, specifically the orientation of the detectors (Fazio et al., 2004)

3.3 IRAC Data Reductions

Raw data from the IRAC instrument are sent through data pipelines, so that they may be properly calibrated. The raw data (labeled Level 0) is received and sent through the first pipeline to create Basic Calibrated Data (BCD), or Level 1 data. The BCD are strictly flux calibrated. The first step in the process is to do a "sanity check," which is a series of checks to make sure that the data files are actual images, and that their parameters match expected values (for instance, the pipeline checks to make sure that the data file's header shows that the shutter was registered as open). The pipeline then goes on to correct for "overwrapping," which comes from practice of discarding the signed data for easier downloading from the SST to the ground. Any negative numbers will therefore appear to be very large positive numbers. Any pixels that have values larger than the physical saturation limit for each detector (45,000 counts in the two wavelengths used in this thesis) are assumed to be overwrapped pixels, and will be corrected to their actual negative number. The data also has to be corrected for "echos," which are a certain pixel's data appearing in another pixel. This arises from the time constant within the cables that connect the detectors to the readout assembly. The echo appears in the next readout pixel. Because the IRAC instrument detectors utilize a 4 channel readout assembly, the next readout pixel will be 4 pixels later.

The dark current is then subtracted out by laboratory-taken dark frames, called lab darks. There are two steps in the actual dark correction process. The first step in this dark correction process takes place before linearization. The data are then linearized, because the detectors are not completely linear over the entire dynamic range. So, as the detector fills with photoelectrons, more

photon strikes are needed to free another photoelectron. For channels 1 and 2, the linearization is handled by a solution to the quadratic equation

$$\mathrm{DN} = \frac{-1 + \sqrt{1 - 4L\alpha\mathrm{DN}_{\mathrm{obs}}}}{2L\alpha} \tag{3.1}$$

where

$$L = \frac{\alpha}{n * (w+n)^2} \left[\left(\sum_{n+w+1}^{2n+w} i^2 - \sum_{1}^{n} i^2 \right) - 2(1 - \frac{t_d}{t_c}) n(n+w) \right]$$

which contains $\alpha = \frac{A}{m^2}$, n is the Fowler number, w is the wait period, and t_d is the time between reset and first pixel readout. The Fowler number is the number of non-destructive reads of a pixel during an exposure. When an infrared detector is reset for the start of a new exposure, n non-destructive reads of each pixel are taken. Once the integration time for the exposure has been reached, another set of n reads is taken, which are then averaged together and subsequently subtracted from the original exposure. This results in a significant reduction in noise (Fowler and Gatley, 1990). For this thesis, the targets were not bright enough for non-linearity to be a concern. Once the data are linearized, it has to go through the second dark subtraction. This is done in a similar process to standard CCD images, utilizing a "delta-dark" frame, which is simply a skydark that has had the lab dark subtracted from it. In addition, the background zodiacal light contribution is estimated and included in the image header, for future analysis.

Next is the standard flat field correction to the data. IRAC uses what is called a "super-skyflat," which is a flat composed of 5 years old flats. The benefit of this is that there is a very high S/N on the flat. A few more simple parts of

the pipeline are applied, which consist of a vertical flipping of channels 1 and 2 data, detection of cosmic rays, and finally a calibration is done to convert the image from DN/s to Mega-Jy/sr. The final step in the first pipeline for most cases is to inject the pointing information into the data file headers. During telescope operations, the pointing of the telescope is monitored at a frequency of 2 Hz throughout a 12 hour span, which is stored in a Boresight Pointing History File (BPHF). At the end of the 12 hour cycle, the BPHF is downloaded from the telescope. During the actual pipeline process, the relevant pointing information is searched for in the various BPHFs and then injected into the header, for use by the user.

This concludes the BCD pipeline for reductions for Level 0 data. Once the BCD is made, they are put through an artifact-correction pipeline to produce Corrected BCD files (CBCD). The artifacts that are generally corrected for are stray light, saturation, and "channel pulldown" for channels 1 and 2. Channels 3 and 4 have another correction to do to remove banding, which is when rows and columns, that have bright sources in them, show a higher flux than the nearby rows and columns. Also to be noted, channels 1 and 2 used to experience "muxbleed" effects, where every 4th column from a very bright source experienced additional flux but, according to *IRAC Warm Image Features and Caveats*, the muxbleed effect was only present in images taken during the transition phase from the cold to warm missions. The muxbleed effect is different from the echoes mentioned earlier because it was only seen in very bright objects, while the echoes are from the time constant of the readout circuitry. But, similarly, the readout mechanism (with every 4th pixel being readout by the same column) caused the muxbleed effect to only be seen in sets of four pix-

els. Because the data of this study were collected after this transitional stage, muxbleeding was not present.

The second pipeline for IRAC data, the Level 2 Pipeline, or "post-BCD" (PBCD), does not do any calibration to the flux. Instead, the PBCD pipeline mainly accomplishes the tasks of refining the pointing for each CBCD file, from the BPHF for each image, into a "super-BPHF," and also mosaicking the CBCD files together. The benefit of mosaicking the images together is that a higher S/N is achieved by averaging overlapping frames of BCD files. The process of mosaicking can only be done with the refined pointing that is calculated. Another benefit is that each mosaicked PBCD file has exactly the same pixel size, which is 0.6 arcsec by 0.6 arcsec. The process of mosaicking is similar to that of "drizzling," where the various BCD files are overlaid onto a larger grid, which is all determined by the super-BPHFs.

For more information on the IRAC instrument, see the *IRAC Instrument Manual Version 2.0.2* and the *IRAC Warm Image Features and Caveats*.

3.4 Sample Selection

The data for all of the targets of this thesis were collected at a 3 day cadence over the span of one year, starting in August of 2011. The cadence was chosen because Seyfert AGN show very little variability shorter than a few days, so the sampling rate doesn't have to be smaller than a few days as well. Over the course of the year, there were several gaps in the temporal coverage for each AGN, which corresponds to instrument downtime. All of the targets had Right Ascension and Declination coordinates that are close to the ecliptic north pole,

defined to be at an RA of 18h00m00s and a Dec of +66d33m38.55s. This helps to minimize the effect of stray infrared emissions from the zodiacal dust that orbits the Sun in the plane of the ecliptic.

The galaxies in the sample were chosen as they are representatives of different types of Seyfert galaxies, ranging from standard Seyfert 1 galaxies to Seyfert 1.9 galaxies (see Table 3.1). The intermediate Seyfert types (1.2, 1.5, 1.9) are Seyfert galaxies that do not exhibit the same relative fluxes of the broad lines to the narrow lines, but still have broad line emissions. As the classification gets closer to Seyfert 2, the flux from the broad lines starts decreasing. At the higher intermediate classifications, such as Seyfert 1.8 and 1.9, the only broad lines that are noticeable are the Hα and Hβ, with the flux ratio of Hα to Hβ becoming much larger than in Seyfert 1s. At Seyfert 1.9, virtually the only broad line that is detected is the Hα (Osterbrock, 1981). Spatially, an intermediate Seyfert galaxy would be a galaxy where the AGN is only partially obscured by the DT, unlike Seyfert 2s which have the entire AGN obscured by gas and dust. Over time, the intermediate classifications have been measured to change, sometimes shifting the classification from a 1.8 to a full Seyfert 2. This change in classification supports the clumpy torus theory, because the clumps in the DT would move into and out of the line of sight observers have on the BLR, obscuring parts of the BLR to observers.

Also, some Seyfert galaxies have such large-scale variability in the broad-line emissions that they have been known to change classification with time. 3C 390.3, one of the target AGN of this thesis, is especially known to be incredibly variable in its emission (Penston and Perez, 1984). The variability is so great that the broad lines can sometimes almost completely disappear, leaving only

the narrow lines. This phenomenon would lead to the AGN being classified as a Seyfert 2 galaxy, if sampled at a particular time.

A Narrow Line Seyfert 1 (NLS1) type galaxy is a Seyfert 1, except that the line emissions tend to be almost too narrow to be classified as a typical Seyfert 1. Usually the Balmer lines are analyzed to determine if the AGN is a normal Seyfert 1 or a NLS1 type galaxy. The cutoff for when an AGN is considered a NLS1 is when the H-β line is measured to have a width $<$ 2000 km/s. Additionally, NLS1 type galaxies have stronger FeII emissions than Seyfert 1s, while also having weak [OIII]λ5007 emissions (Komossa, 2008, and references within). This indicates that a portion of the BLR in NLS1 AGN is fully ionized and optically thin to the continuum photons (Rodriguez-Pascual et al., 1997). NLS1 type galaxies appear to have high accretion rates (near the Eddington accretion limit, which is the accretion rate needed for the luminosity of the accretion disk to be at the Eddington Luminosity) and low SMBH masses, which means that they might represent the early stages of AGN.

Table 3.1: Basic information for targets of Reverberation Mapping, from Axon et al. (2011). Other information was obtained from NED.

Target	Position (J2000)	Flux Density (mJy)	Redshift (z)	Classification	$L_{optical}$ ($L_{\odot}$)
3C 390.3	$18^h42^m09.0^s$ +79°46'17"	23	0.056	Seyfert 1.5	2.93 x 10^{10}
AKN 524	$17^h36^m53.3^s$ +68°10'17"	3	0.024	Seyfert 1.5	1.2 x 10^{10}
IRAS17552+6209	$17^h55^m40.4^s$ +62°09'41"	7	0.084	Seyfert 1.9	2.18 x 10^{9}
KAZ 102	$18^h03^m28.8^s$ +67°38'10"	13	0.136	Seyfert 1.2	1.04 x 10^{11}
KAZ 163	$17^h46^m59.8^s$ +68°36'37"	8	0.063	Seyfert 1	4.17 x 10^{10}
MRK 507	$17^h48^m38.4^s$ +68°42'16"	14	0.056	Narrow Line Seyfert 1	5.33 x 10^{10}
MRK 876	$16^h13^m57.2^s$ +65°43'10"	30	0.129	Seyfert 1	2.33 x 10^{11}
MRK 885	$16^h29^m48.2^s$ +67°22'42"	18	0.025	Seyfert 1.5	3.48 x 10^{10}
NGC 6418	$17^h38^m09.3^s$ +58°42'54"	12	0.029	Seyfert 1	2.26 x 10^{9}
PGC 61965	$18^h30^m23.1^s$ +73°13'10"	94	0.123	Seyfert 1	3.55 x 10^{11}
RXSJ19091+6652	$19^h09^m10.9^s$ +66°52'21"	7	0.191	Narrow Line Seyfert 1	7.63 x 10^{10}
UGC 10697	$17^h02^m44.3^s$ +72°53'30"	3	0.053	Seyfert 1	6.93 x 10^{10}

Chapter 4

Data Analysis

4.1 Photometry

The photometric analysis of the targets was handled by the Mosaicker and Point Source Extractor (MOPEX), which is the data analysis software package developed by the Spitzer Science Center for use by the SST. The MOPEX package was designed specifically for SST, but because it does not use any SST specific architecture, it can be readily adapted for use in data analysis of any telescope (Makovoz and Khan, 2005). MOPEX's main functionality, image mosaicking, is especially useful for SST, due to the way SST completes an observation: it takes multiple images of the target by moving the telescope in small amounts, so that each image has a different section of the area around the object. For this thesis, each observation in each channel was composed of 10 of these "sub-images."

Image mosaicking is the process of "stitching together" numerous images

to make one composite image. The reason this is done in astronomy is that by doing this, astrophysicists can improve the quality of the data by reducing noise and error in the composite image. MOPEX will also correct the images for geometric distortion (which the SST suffers from) while also performing outlier rejection on the images, which is very necessary for space-based observatories. Cosmic rays are very prolific in space-based observations, and so outlier rejection is utilized to get rid of them; the basic idea being that any pixels that have significantly higher photon counts in them than the surrounding pixels are considered outliers, and are removed from the image.

There are other ways to make composite images for use in astronomical observations. The simplest one is known as "shift and add" image processing. The basic idea of shift and add is that many shorter exposures of the target are taken, with each observation being shifted around by an amount of pixels (in a process called dithering), so that the target is in a different position in each observation. Once all of the observations have been made, the composite image is constructed by shifting each image around so that they are all lined up. The images are all averaged together afterwards, to make one image. The idea behind this technique is that by averaging the images together, the actual measured photometry from the star is subject to less variation, and will therefore be closer to the true value for the target. Shift and add image processing is a simplistic form of image processing. It does not correct for optical aberrations in the telescope, which means that other image processing techniques are needed in order to correct for the aberrations. Typically, shift and add is used over subpixel shifts, rather than full pixel shifts, because this subpixel sampling allows astrophysicists to observe structures and details that otherwise would've

been impossible to observe.

A second, common image processing technique is called interlacing. Interlacing takes the input images, which have been dithered, and assigns each pixel on the original input image to an alternate pixel on an output image. This is accomplished by calculating the how the centers of targets are aligned in the input images. The major downside to interlacing is that the dithering of the images must be very accurate, otherwise the input pixels get mapped to incorrect output pixels. Additionally, geometric distortions in the optical system will produce the same effect as inaccurate dithers.

A more refined image reconstruction technique is called Variable-Pixel Linear Reconstruction, also known as "Drizzle." Drizzle works as a middle ground to both shift and add and interlacing. The algorithm first takes the input images and maps each pixel, in each input image, to an output pixel, taking into account any corrections for image distortions. These output pixels are usually smaller in size than the input pixels. Once this mapping is complete, the algorithm then shrinks the input pixels. The reason for this is to prevent reconvolution of the new image with the pixels of the input. Once the pixels have been shrunk (by a scaling that is chosen by the astrophysicist), the Drizzle process will then begin to average the flux in each output pixel by accounting for only the input pixels that overlap the output pixel. Additionally, each input image gets statistically weighted, which also determines how much flux is contributed to the overall output. The weighting takes into account detector noise, distortions, and cosmic ray hits (Fruchter and Hook, 2002). The technique is shown in Figure 4.1.

Drizzle is best used on images that are undersampled across the field of view. Undersampling is what happens when the limiting factor of an observer's

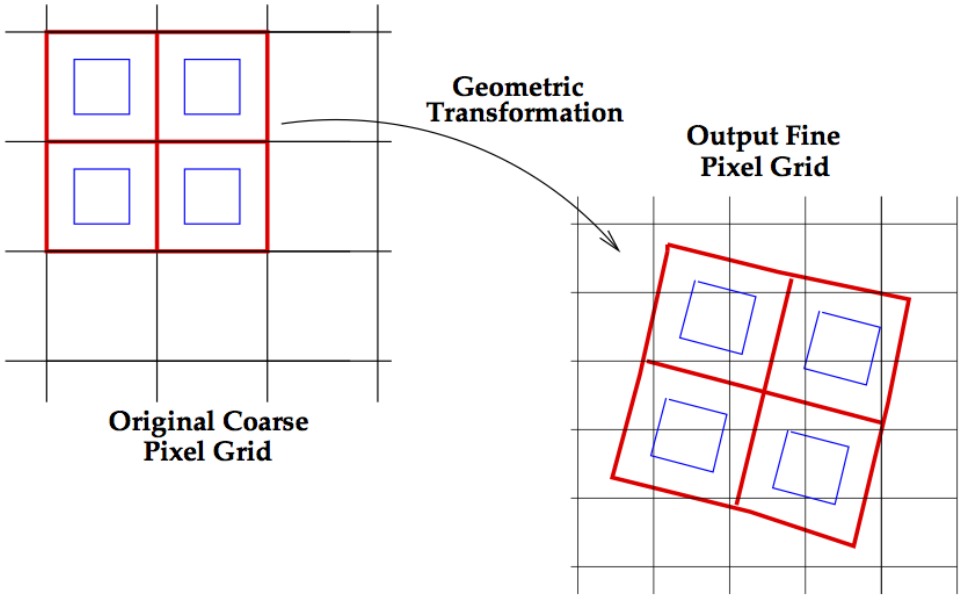

Figure 4.1: A visual representation of how the Drizzle technique works. Red lines deliniate the original pixels, while the blue lines deliniate the pixels after shrinking. In the output pixel grid, only pixels that contain a portion of a shrunken input pixel will have flux associated with them (Fruchter and Hook, 2002).

resolution is the detector being used. When a field is undersampled, the pixels in the detector are larger than the angular resolution that satisfies the Nyquist criteria for the object being observed. To satisfy the Nyquist criteria, the pixel size of the detector has to be half the size of the angular resolution of the telescope itself. Typically, when designing telescopes, astronomers must choose between either having an optimally sampled, small field of view or having an undersampled, larger field of view. Drizzle was originally designed to be utilized on the Hubble Deep Field, which was taken using the Wide Field and Planetary Camera 2 (WFPC2). The WFPC2 does suffer from undersampling, and so the Drizzle technique is used to more accurately recover the data. Drizzling can be useful on data obtained from IRAC, but not by much. Typically, drizzling will reduce the point-response function (PRF) of a point source by about 10%, with the downside that it also creates an unevenly weighted IRAC image. Because the targets were all at the center of the IRAC, the sampling was the best, and so drizzling was not performed.

Additionally, MOPEX also handles the photometric data analysis on each image. This function can be turned off, if only the mosaicked images are necessary. MOPEX handles photometry in a few different ways. MOPEX will automatically perform both aperture photometry and point source extraction. Point source extraction is done on the subimages of an observation, and involves fitting a point-spread function (PSF) to all detected sources in the subimage. Once the PSF is fit to each source, the amount of flux that is contained in the point source can be calcuated. PSF-fitting is a very accurate way to measure the fluxes of point sources, but is not useful for fitting extended sources, such as Seyfert galaxies. Because this thesis handles mostly Seyfert galaxies, PSF

extraction was not utilized.

Aperture photometry is done on the final mosaics, not on the individual subimages. The basic idea behind aperture photometry is that an annulus around a source is used to calculate the flux from the source. This method is better for extended objects, as it calculates the total flux within an area, and so it is not dependent on spatial orientation and shape. The flux follows the basic equation

$$F_{\text{obj}} = F_{\text{inner}} - F_{\text{sky}} * N_{\text{inner}}$$

The object's flux (F_{obj}) is calculated by first measuring all of the flux that falls within a certain radius of the object (F_{inner}). This radius is the inner radius of the annulus. Once the flux in the inner radius has been measured, a second, larger radius is then used. Instead of measuring the flux in the total area of the outer radius, instead only the flux that is in the area bounded by the inner and outer radii is used (F_{outer}). This flux is then divided by the total number of pixels in the outer area (N_{outer}) to get the sky contribution (F_{sky}) per pixel.

$$F_{\text{sky}} = \frac{F_{\text{outer}}}{N_{\text{outer}}}$$

Once the sky contribution has been calculated, then the total amount of sky flux within the inner radius ($F_{\text{sky}} * N_{\text{inner}}$, where N_{inner} is the number of pixels in the inner radius) is subtracted from the total inner flux to arrive at the flux of the object. The term "sky contribution" is a catchall phrase, used to describe dust and other material that is between the object and the telescope. For ground based telescopes, the sky itself is not perfectly dark, and so there is a relatively uniform brightness that will add photons to the detector in all

pixels. For aperture photometry to work, the outer area needs to be totally clear of bright sources of photons. In space, the zodiacal dust's scattering is a large source of excess photons in the detector.

MOPEX generates data files for each observation, which must be parsed through in order to generate a light curve. This was done via a Python script written specifically for this purpose. Each point source in the file is paired with its position on the sky, so the script was written to take an input position and search through the entire file until the same position is found. Due to proper motion and to pointing errors with the SST, a very small range (of order 10") was given in order to find the source. An arbitrary instrument SNR minimum (50) was also included, in order to eliminate false identifications. This position search was done using the Astropy package, designed specifically for astronomical research (Astropy Collaboration et al., 2013). Once the target was found in an observation, the time of observation, flux, and uncertainties were stored into a temporary Numpy array until each the target had been found in each observation. If the target was not found, that observation had zeros for the flux and uncertainty. Once all observations were searched, the Numpy array was saved into a file. This process was done for each channel, for each target.

4.2 Cross Correlation

In order to measure the time lag between the two channels, the data had to be cross correlated. Cross-correlating two functions results in a measurement of how the two functions are phase shifted from each other. If the first function is shifted ahead of the second, the cross correlation yields a positive shift, whereas

if it is shifted behind the second, the correlation yields a negative shift. In order for the two functions to be accurately correlated, they must be similar to each other (Press et al., 2007). This signal analysis is very useful for this thesis, because the light curves between the two channels are expected to be very similar functions, with some time lag between the two. This lag is measured as a shift between the two light curves. In order to calculate the normalized cross correlation C_{xy}, which is a function of time lag τ, first the unnormalized cross correlation r_{xy} is calculated via the equation

$$r_{xy}(\tau) = \frac{1}{N} * \sum_{k=0}^{N-\tau} (x(k) - \bar{x}) * (y(k+\tau) - \bar{y}) \tag{4.1}$$

where x and y are functions, N is the total number of data points in each light curve, $\bar{x}$ and $\bar{y}$ are the means of the functions, is used. C_{xy} is then calculated by

$$C_{xy}(\tau) = \frac{C_{xy}(\tau)}{\sigma_x * \sigma_y} \tag{4.2}$$

where σ_x and σy are the standard deviations of the functions (IBM Corporation, 2013). Using these equations will calculate only the positive lags, so Equation 4.1 must be modified to

$$r_{xy}(\tau) = \frac{1}{N} * \sum_{k=1}^{N-\tau} (x(k) - \bar{x}) * (y(k-\tau) - \bar{y})$$

in order to calculate the negative lags.

Cross correlation has the caveat that the data must be well-sampled and continuous. Unfortunately, for all of the targets the first half of the data in all sets have multiple gaps in the light curves. So, the whole light curve could

not be used. There was a large enough subset at the end of the curves that was continuous across the sampling rate. All of the targets were also well-sampled with a very strict sampling rate of one observation every three days. Theoretically, if the data were cross correlated as is, then the sampling resolution would be no less than three days. In order to combat this, the data are linearly interpolated between the actual data points, so that the effective resolution of the light curves is one day between observations. This is a form of upsampling, which increases the sampling rate of a discrete signal. In order to be able to do this, without introducing error, the signal that is being interpolated can not have large variances on time scales smaller than the original sampling rate. Interpolation allows a cross correlation algorithm to return time lag values that are smaller than the original resolution (in this case, three days). The procedure for this is to interpolate channel 2's time curve, and then cross correlation the actual data points in channel 1 with the interpolation of channel 2. Once this is done, the process is repeated, but this time channel 1 is interpolated and channel 2's actual data points are used. Once both correlations has been run, they are averaged together to get an overall cross correlation for both light curves.

4.2.1 Test Case

A test of the cross correlation method was done, utilizing two sine curves. The first test was a simple test to see if the algorithm could recover the phase difference between two identical sine curves, which were both $x = y = sin(i)$, where $i = [-6\pi, 6\pi]$. As expected, the algorithm recovered a phase difference of 0, as shown in Figure 4.2(a). For the second test of the algorithm, in Figure 4.2(b), gaussian noise was added to each signal so that the signal to noise ratio

(SNR) would be 10, which the algorithm was able to recover. SNRs of 5, 2, and 1 were additionally tested. An SNR that is this low is not expected for the data, but is useful to see when the algorithm fails. SNR tests of 2 and 1 are in Figures 4.2(c) and 4.2(d) respectively, while the SNR 5 test is not shown, as it was functionally identical to the 10 SNR test.

The second set of tests of the algorithm involved adding a known phase difference to the sine curves. The phase difference that was added was $\pi/3$, so that $x = sin(i), y = sin(i + \frac{\pi}{3})$. Each curve was made up of 200 points spanning 12π radians, which equates to $\frac{\pi}{3} = 5.5$ data points on the cross correlation, so the algorithm should return either 5 or 6 as the difference. The algorithm calculated that the phase difference between the two curves, with no noise added, was -5, which is consistent with what was predicted. The difference was -5, because with a positive phase difference, the second curve leads the first curve, which makes the algorithm recover a negative difference, because it calculates the correlation with respect to the first curve. Figures 4.3(c) and 4.3(d) were similar to those in Figure 4.2. As in the first case, there was virtually no difference in the correlations of the 10 SNR and the 5 SNR test cases.

What these tests show is that the algorithm is able to recover phase differences between two light curves, provided that the SNR of the light curves is no less than 5. This is completely acceptable, as the SNR of the data is predicted to surpass this threshold.

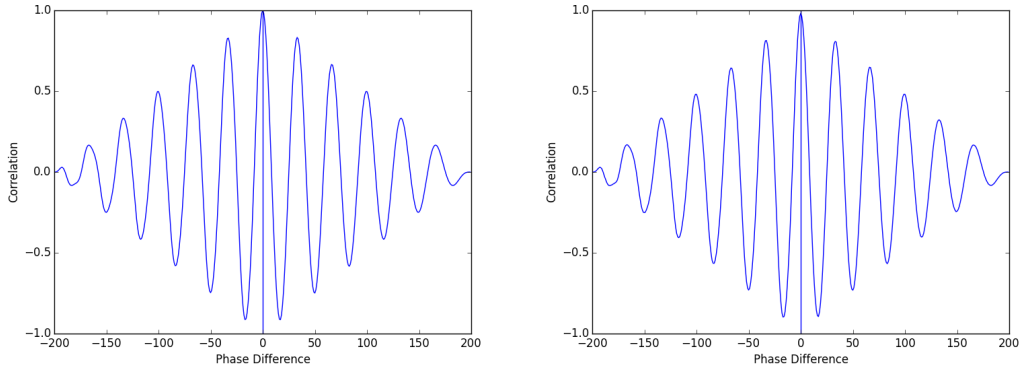

(a)

(b)

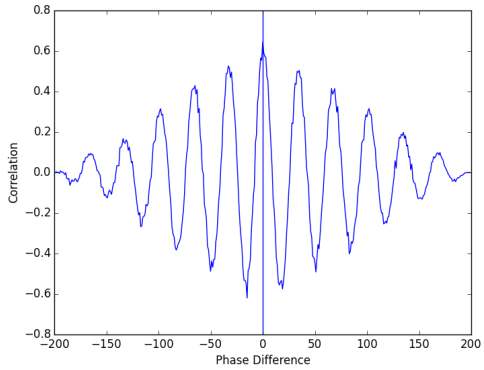

(c)

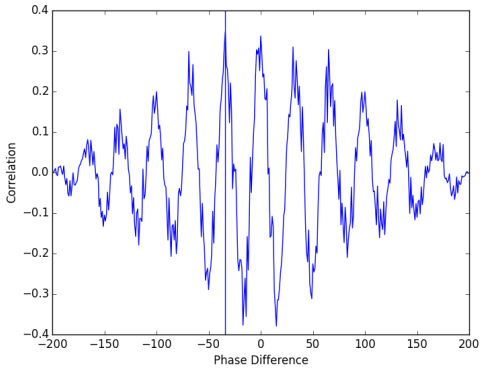

(d)

Figure 4.2: (a) The cross correlation of two sine curves with no noise or phase difference added. (b) The same curves with a 10 SNR noise added. (c) At an SNR of 2, the algorithm started to recover false phase differences. (d) An SNR of 1 yields no useful data.

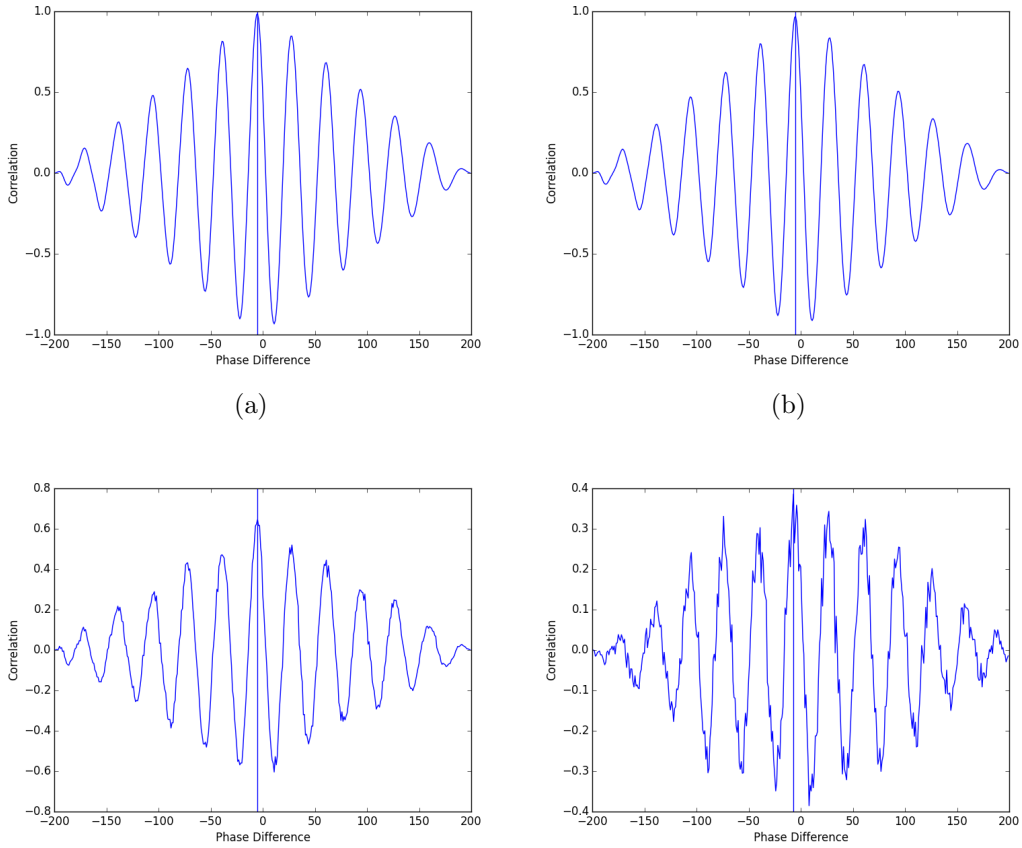

Figure 4.3: (a) The cross correlation of two sine curves with a phase difference of $\frac{\pi}{3}$ and no noise added. (b) The same curves with a 10 SNR noise added. (c) At an SNR of 2, the algorithm started to recover false phase differences. (d) An SNR of 1 yielded a phase difference that was close to the actual difference, but was still wrong.

4.3 Flux Randomization/Random Subset Selection Method

Doing a straight cross correlation of two light curves will yield only a static measurement of the correlation, with no way to determine the error associated with the cross correlation. The method known as Flux Randomization/Random Subset Selection (FR/RSS) was developed in order to characterize the uncertainties (Peterson et al., 1998). The method is composed of two separate methods themselves, Flux Randomization and Random Subset Select. The first portion utilizes the errors on the measurements of the light curves. For each datum in a light curve, there has to be an associated error. In order to accomplish the FR portion of FR/RSS correctly, each datum, on the original light curves, is modified by a random amount that conforms to a gaussian selection utilizing the uncertainty as the sigma with a mean of zero (so that the light curve is, on average, not disturbed from the original light curve). This new light curve is artificial in nature, but is carried through to the next step. The second stage, RSS, is similar to the statistical process of "bootstrapping." For a pair of light curves with N data points, a subset of N pairs will be randomly selected from each light curve, so that each data point selected is represented in both light curves. Each random selection is made without regard to prior selections. At the end of the selection, some points on the constructed curve will have been selected multiple times, while some points will not have been selected at all. The RSS process is utilized to determine how important any one point is in the actual cross correlation.

Once two light curves have been made via the FR/RSS method, they are

cross correlated. The peak of the cross correlation is then recorded for later use. Next, another set of light curves was made using the FR/RSS method and cross correlated. This was repeated 2000 times, until a distribution of cross correlation peaks has been constructed. The median of the cross correlation peak distribution (CCPD) is taken to be the actual time lag between the two original signals. The CCPD can not be assumed gaussian, so the easiest way to measure the lag is to calculate the quartiles of the distribution (the points in the time-lag space of the distribution where 25% of the data and 75% of the data lie). These quartile positions are then assumed to be the measure of the error (subtracting the time lag of the 3^{rd} quartile from the median yields the upper error and subtracting the median from the time lag of the 1^{st} quartile yields the lower error).

Chapter 5

Results

The results from each NIR cross correlation are below. The longer wavelength was cross correlated with the shorter wavelength, so that in effect the algorithm searched the longer wavelength for the same signal found in the shorter wavelength. If the signal was found in the longer wavelength, then there will be an associated time lag with the signal. A positive time lag means that the longer wavelength precedes the shorter wavelength, with a negative lag meaning the reverse. The longer wavelength is expected to lag behind the shorter wavelength, because the warmer dust is expected to be closer to the AGN continuum than the cooler dust (i.e. the 3.6 μm emission-clouds are expected to interact with the continuum photons before the 4.5 μm emission clouds). Additional information about the target in question is also provided. Each light curve had gaps in the observations, and so therefore all data that is previous in time to the last gap is not used in the correlation. The dating system used by SST observations is called the Modified Julian Date (MJD), which is the Julian Date (JD) - 2400000.5. The JD is the system of measuring days, starting at noon,

on 1 January 4713 BCE. Typically, JDs are used as they allow easy calculation between dates. JDs are also used by astronomers as a precise form of time measurement. The MJD is used in order to ease loads on data transmission, as less bits are needed to be transmitted if MJD is used versus JD. Additionally, each light curve was normalized.

5.1 3C 390.3

The AGN 3C390.3 is an FR II radio-loud galaxy that exhibits broad line emissions. The broad line emissions in the core would identify the AGN as a Type 1.5. Historically, 3C390.3 has shown to have variability similar to radio-quiet AGN, and so is one of the few radio-loud AGN that has been studied for variability surveys (Dietrich et al., 2012, and sources found within).

3C 390.3 had some gaps in the observations, so the cross correlation could only be done on the last portion of the data, starting at an MJD of 55928. The SNR for channel 1 was 102 and the SNR for channel 2 was 104. The cross correlation did not recover a distinguishable time lag from the observations because there were multiple peaks within the CCPD.The multiple peaks are due to the FR/RSS method of cross correlation; each realization has a random subset of data points. When the cross correlation is run, the missing data points will affect the lag between the two light curves. If a data point is important (such as the data point at the beginning of a variance), then not having the data point would drastically skew the results. If there were multiple significant peaks, such as found in 3C 390.3's CCPD, then there was not a distinguishable lag recovered for the AGN.

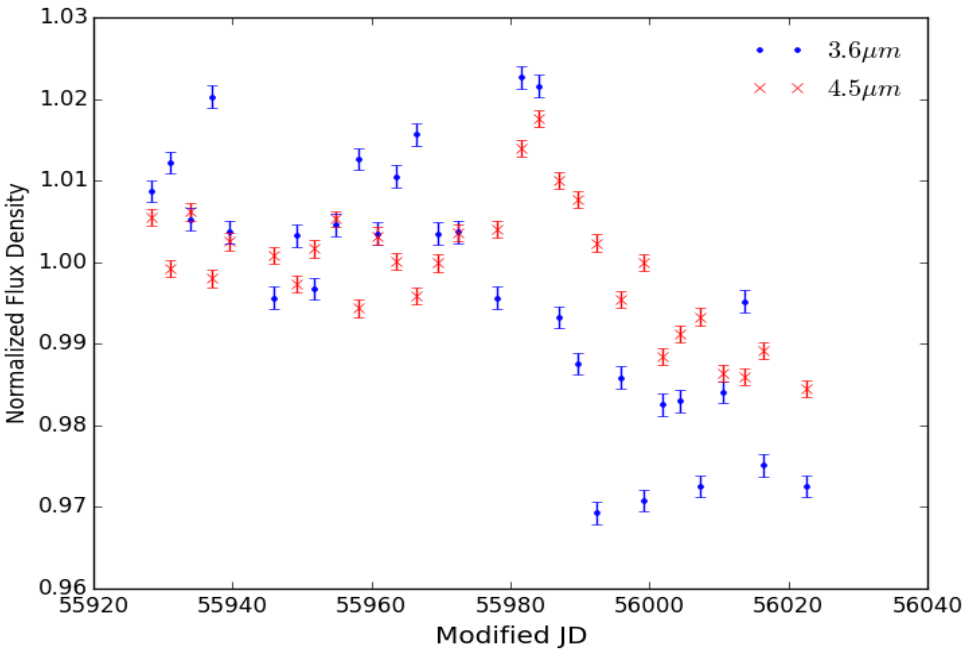

(a)

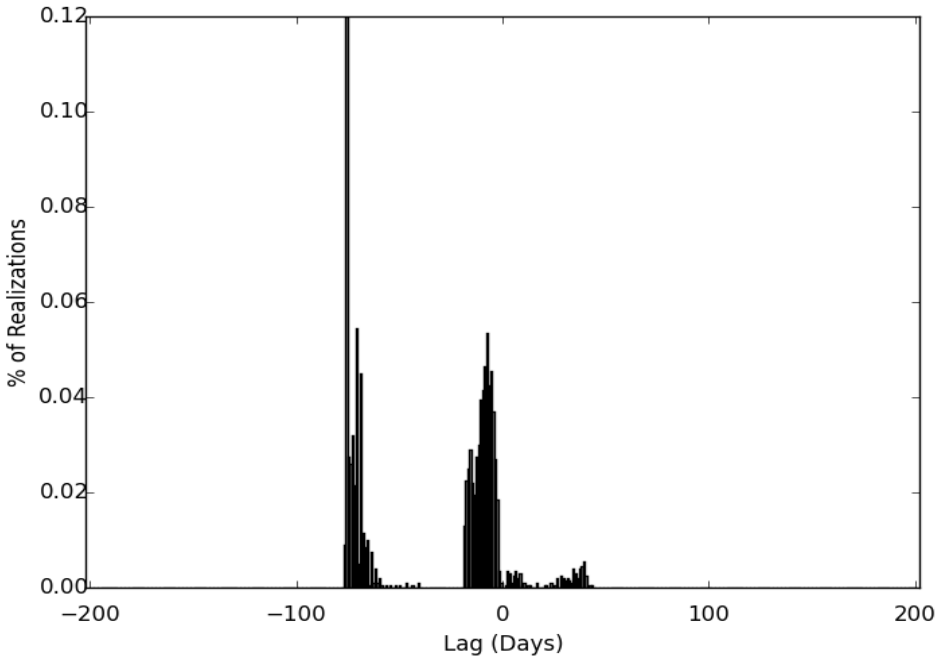

(b)

Figure 5.1: (a) The light curve of 3C 390.3. (b)The CCPD of 3C 390.3.

5.2 AKN 524

AKN 524 is a Seyfert 1.5 type AGN. But, AKN 524 is, historically, not as variable as 3C 390.3. AKN 524 (NGC 6423) has another galaxy paired with it, NGC 6419. This pairing does not mean that they are gravitationally interacting, just that they are near each other on the sky. AKN 524 is fairly unremarkable, because it is very faint, small, and round.

The relatively flat looking light curves for AKN 524 had two small gaps in the data, which precluded the whole light curve from being used. The SNR for channel 1 was 101 and the SNR for channel 2 was 72. Channel 1 was missing data for MJD 55885, so that data point was removed from both channel 1 and channel 2. But, because that would have left a gap right at the beginning of the data that was to be used for the cross correlations (starting at MJD 55882), the extra data point was also removed from both channels. There was no detectable lag.

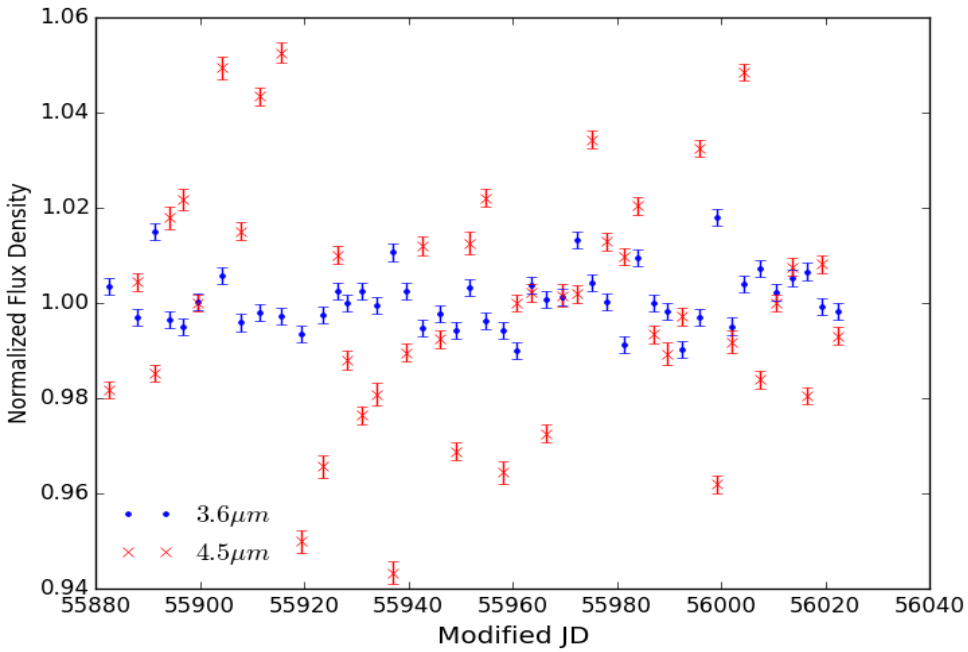

(a)

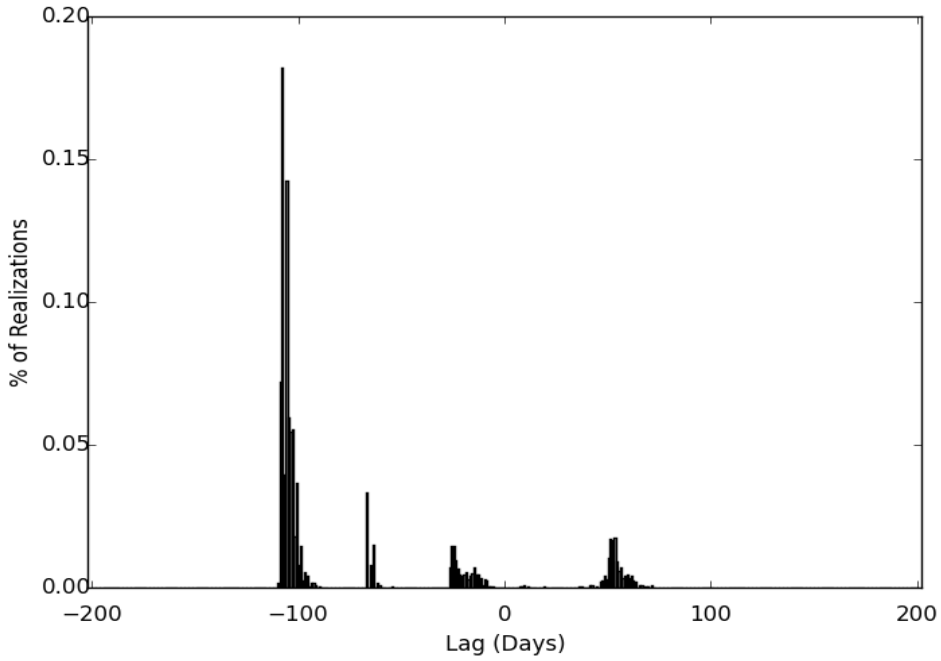

(b)

Figure 5.2: (a) The light curve of AKN 524. (b) The CCPD of AKN 524.

5.3 IRAS17552+6209

IRAS17552+6209 is an AGN of type Seyfert 1.9, which means that it is closer to a Seyfert 2 AGN than a Seyfert 1 AGN. At this classification, only the Broad H-α emission may be seen; the other broad emissions are obscured by the DT. There has been debate on whether IRAS 17552+6209 is a Sy 1.9 or an Sy 2 type AGN. This actually lends credence to the idea of it being classified as a Sy1.9 type, because the intermediate types should vary between being a Sy 2 and almost Sy1; the historical variance in IRAS 17552+6209 almost guarantees that it is in fact an intermediate type.

While the data from channel 1 was consistent throughout the curve, the data from channel 2 was not. The flux levels in the first half of the light curve are significantly lower than the rest of the light curve. This probably stems from some image processing error. Likely, the target was on the border of an image that was mosaicked, and so had some distortions added to it. There also may have been readout errors, but this is unlikely, as readout errors are mostly transient, and would not persist over the course of about 60 days. Additionally, because the error was contained within the part of the light curve that would have been unused anyways, it was thrown out completely. The SNR for channel 1 and 2 were 90 and 82, respectively. Because of the gaps in the data, only the data after MJD 55882 was used. The CCPD of IRAS 17552+6209 contains a sharp peak at -112 days, with smaller peaks in the CCPD at -10 and +55 days as well. There was no detectable lag from IRAS 17552+6209.

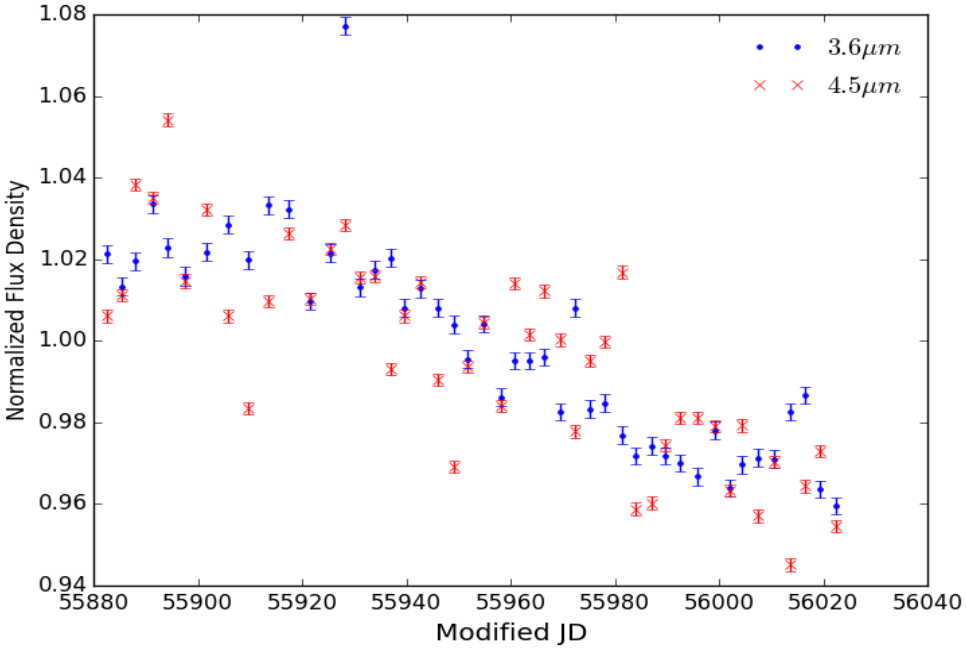

(a)

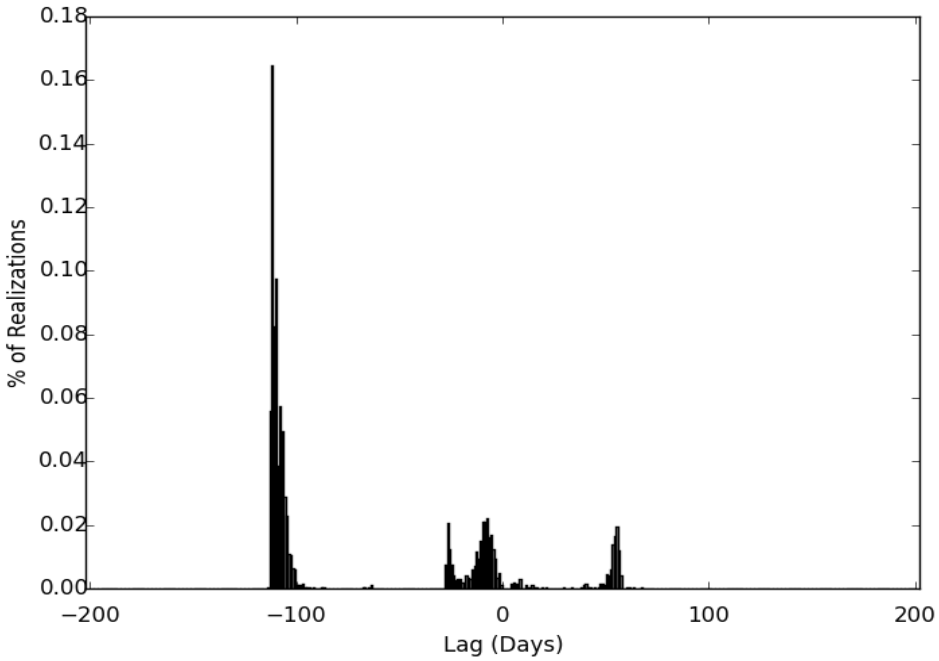

(b)

Figure 5.3: (a) The light curve of IRAS 17552+6209. (b) The CCPD of IRAS 17552+6209.

5.4 KAZ 102

KAZ 102 is an AGN that is classified as a radio-quiet quasar that has a very strong X-ray component and a low redshift. The flux from the core of the QSO dominates the overall flux from the galaxy, but the host can be resolved to an elliptical galaxy. This is an outer halo of the host galaxy that has been detected to be disturbed; this disturbance has been hypothesized to be the final stages of KAZ 102 absorbing another smaller companion galaxy. KAZ 102 also has a companion that appears to be an inclined spiral galaxy (Hutchings and Neff, 1992).

KAZ 102's light curves had gaps in the data up to MJD 55928, so all data before then was not considered for the cross correlations. Channel 1 had more spread in its data points than channel 2. Additionally, the SNR for both channels was 46. KAZ 102 had three distinct peaks in its CCPD. There was a large negative peak, plus a wide positive peak. The third "peak" was also negative, but it was more like a swath of time lags that had around the same probability of happening. No lag was able to be detected.

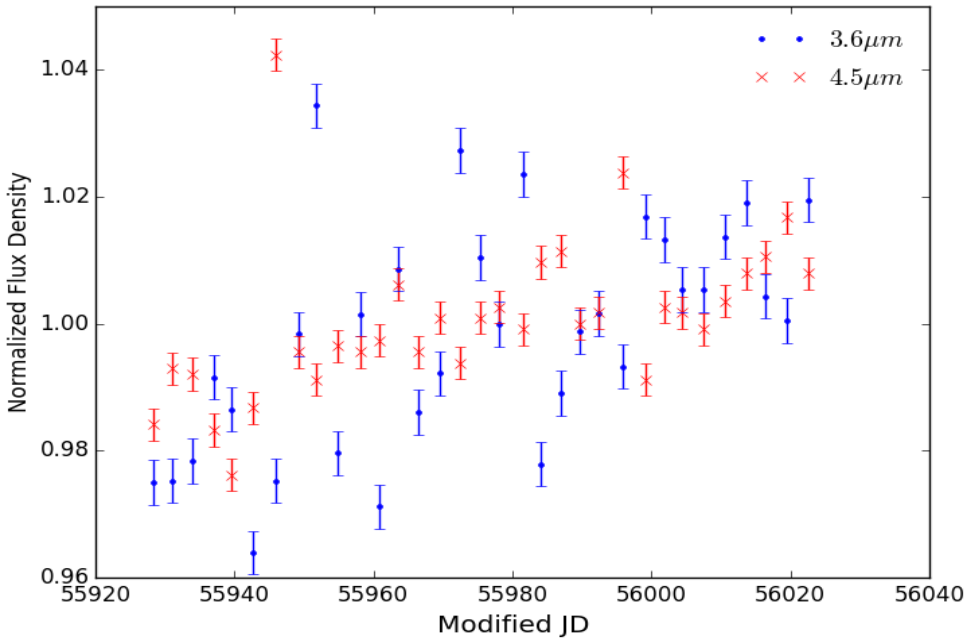

(a)

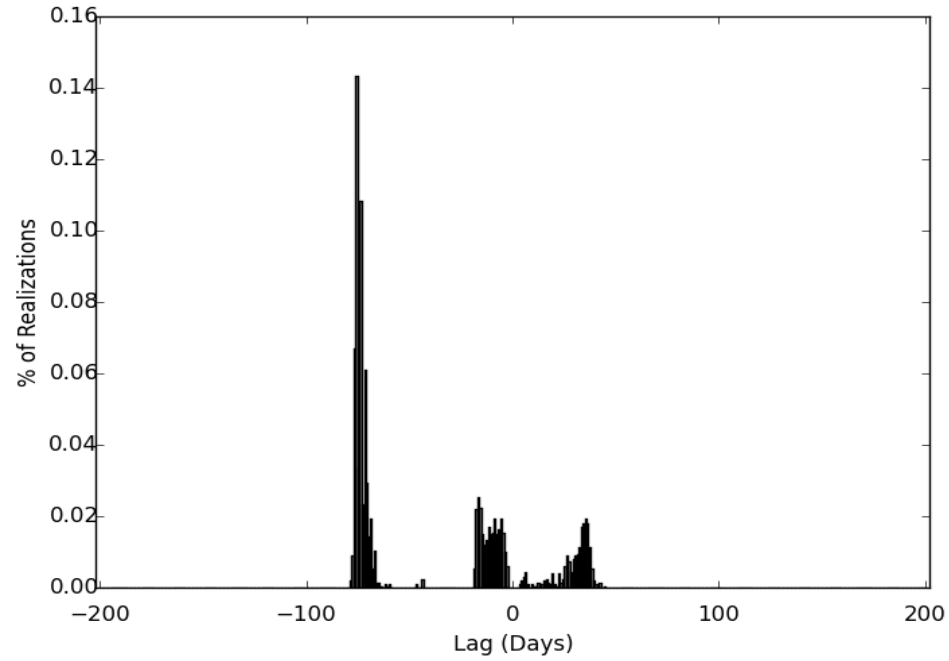

(b)

Figure 5.4: (a) The light curve of KAZ 102. (b) The CCPD of KAZ 102.

5.5 KAZ 163

KAZ 163 is currently colliding with another galaxy, which is known because both objects are at the same redshift. Between the two objects, only KAZ 163 is an AGN (Kriss and Canizares, 1982). KAZ 163 shows emission lines similar to other Seyfert 1 galaxies, whereas the companion has a uniform red continuum (Hutchings and Hickson, 1988). They also found that the companion does not has a rotation curve. There is a third galaxy that might possibly be interacting with KAZ 163, but the signal from that galaxy is very weak, and no emission lines were found.

All data before MJD 55882 was not considered for the cross correlations of KAZ 163. KAZ 163 had a similar problem as IRAS 17552+6209, in that the data from channel 2 was unusable before MJD 55882. As with IRAS 17552+6209, there was most likely an issue with the location of KAZ 163 on the detector for channel 2. There were also dates, within the section of data that was used, where the channel 2 data was missing. These data points were manually removed from channel 2's light curve, while the corresponding data from the same observations were removed from channel 1, to preserve overall integrity. The SNR for both channels was 171. Except for a large spike in the most negative peak, KAZ 163 had 3 distinct, relatively equal peaks in the CCPD. An additional fourth section of the CCPD had a small peak in it, but it is too small to be significant. No lag could be seen in KAZ 163.

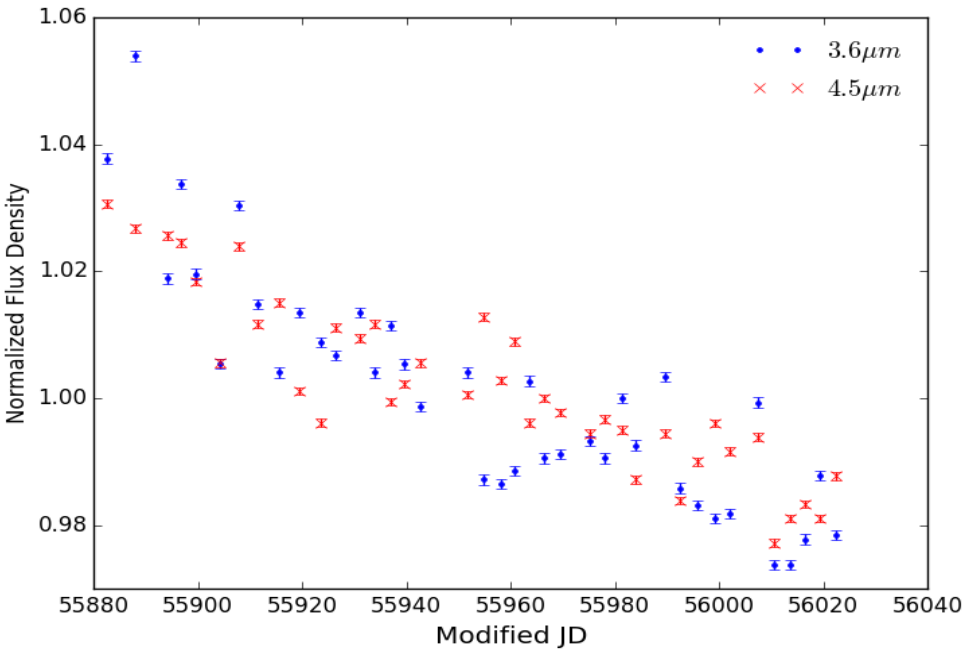

(a)

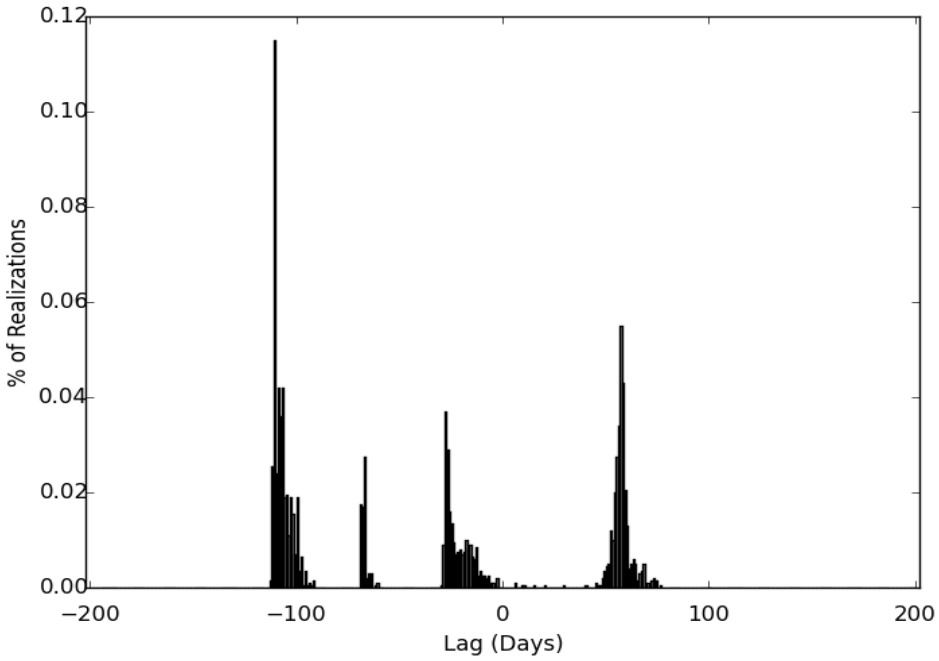

(b)

Figure 5.5: (a) The light curve of KAZ 163. (b) The CCPD of KAZ 163.

5.6 MRK 507

MRK 507 was originally classified as a Seyfert 2 galaxy, but was later reclassified as a Narrow Line Seyfert 1 (NLS1) type galaxy (Halpern and Oke, 1987). This is an easy mistake to make, as NSL1 AGN tend to have no broad Balmer lines, which are the lines that are most often used to identify a Seyfert 1 AGN. It has also been misclassified as an H II region as well, due to the fact that the emission lines can be fitted with a gaussian component that also fits an H II region, in addition to a broad gaussian component. Additionally, the H II misclassification also stems in part from the fact that the emission lines away from the AGN are similar to those found in H II clouds (Véron-Cetty et al., 2001, and sources within).

Only the data after MJD 55928 was used in the cross correlation, with channel 1 having an SNR of 38 and channel 2 having an SNR of 35. MRK 507 had three peaks in its CCPD. The primary peak is at a high negative lag. Both of the two main peaks do not contain a large majority of the correlation realizations, therefore, MRK 507 does not have a lag that is discernible in this thesis.

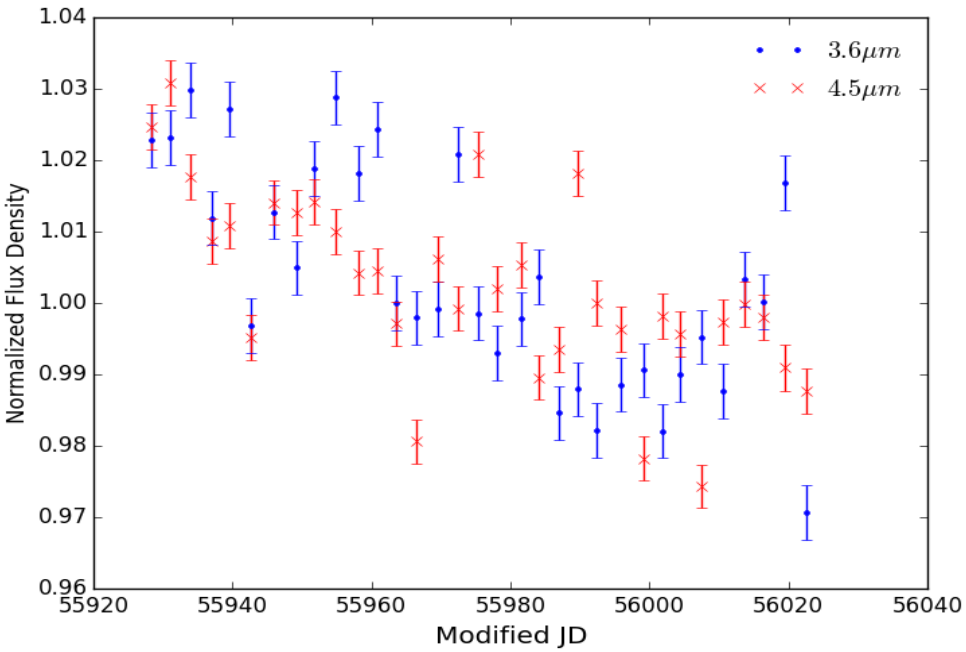

(a)

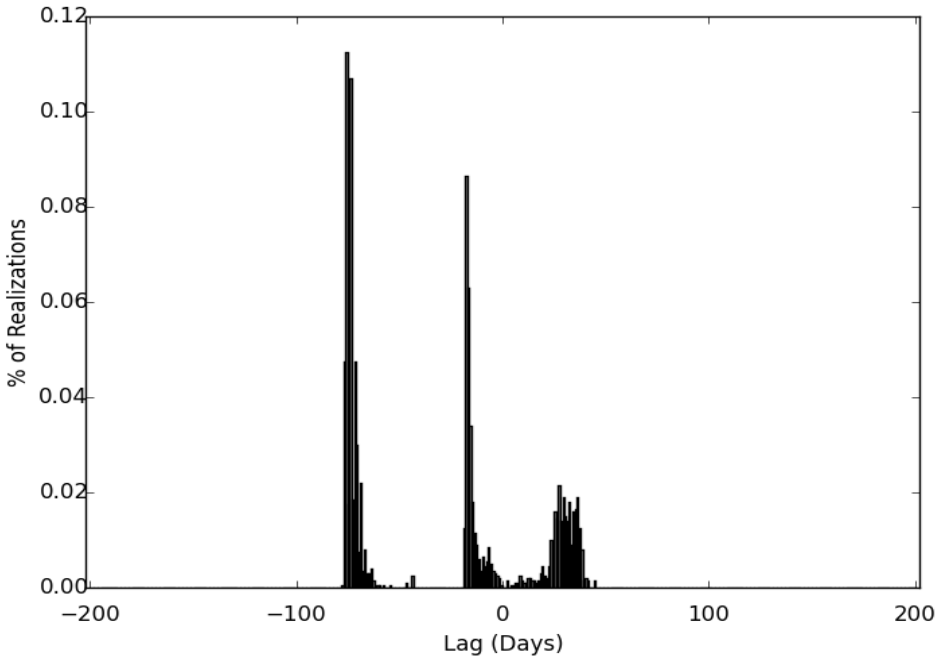

(b)

Figure 5.6: (a) The light curve of MRK 507. (b) The full CCPD of MRK 507.

5.7 MRK 876

MRK 876 is a quasar at a redshift of z = 0.129. Broad nuclear emissions have been detected from the quasar, which would make it a Type 1 AGN. The interesting thing about MRK 876 is that a spiral galaxy, about 20″ away from the quasar, is at the same redshift. There is also a long tail, on the quasar, which is connected to a second nucleus (in projection). The second nucleus was found through plotting isophotes of the quasar (Yee and Green, 1987). According to Yee and Green (1987), all of the evidence points to the quasar and companion galaxy as gravitationally interacting, which has spurred star formation in the nebulous gas found in the vicinity of the galaxies. The interaction is also what probably started MRK 876's AGN.

MRK 876, which had the correlations start at MJD 55928 due to the gap that spans about 100 days, was found to have two large peaks in its CCPD.The measured SNR for channels 1 and 2 were 82 and 84, respectively. MRK 876 was one of the few AGN found to not have a peak in their CCPD at a high negative lag. Even with this, the fact that there are multiple peaks precludes a definitive time lag from being found.

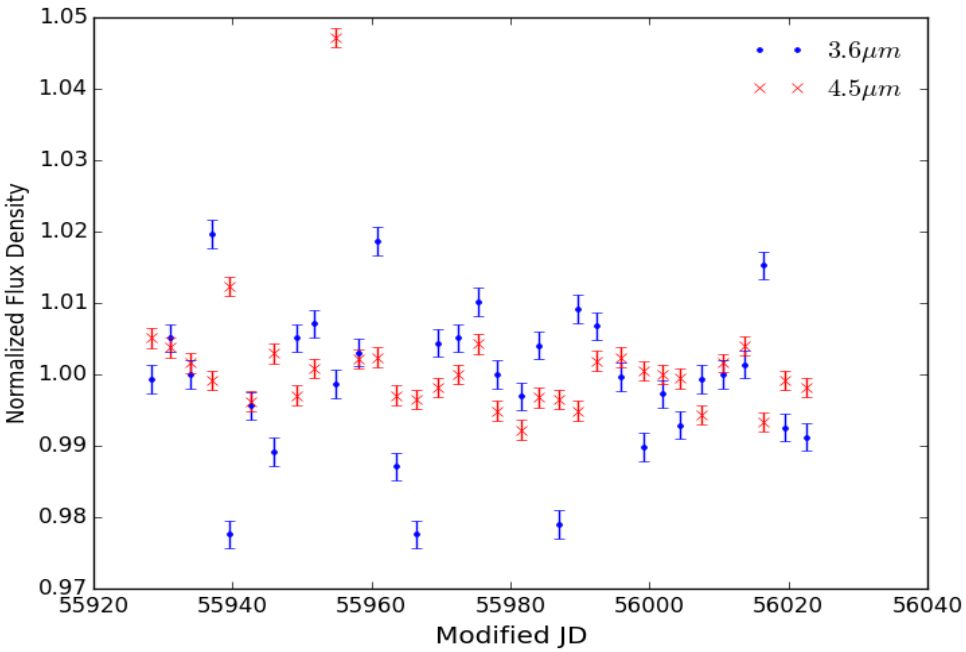

(a)

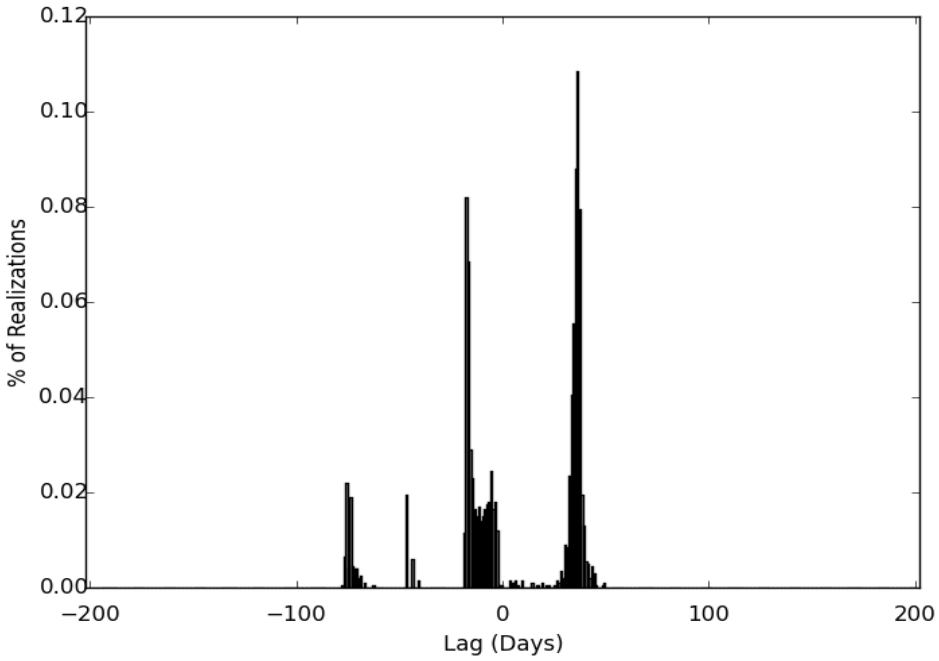

(b)

Figure 5.7: (a) The light curve of MRK 876. (b) The CCPD of MRK 876.

5.8 MRK 885

MRK 885 is a Seyfert 1.5 galaxy located at a redshift of z=0.025, making it the second closest target. Because it is part of the Markarian catalog, it has a large UV component in its spectrum, which is attributed to non-thermal emissions. Its spectrum was found to contain stellar absorption features (Jiménez-Benito et al., 2000). Photometric analysis, specifically via isophotal and surface-brightness analyses, has shown that MRK 885 contains a bar in the nucleus, and that the nucleus may contain a spiral arm (Xanthopoulos and De Robertis, 1991).

Due to the gaps in the light curves, only the data points starting on MJD 55928 were correlated. The SNR for channel 1 was 31 and the SNR for channel 2 was 25. The light curves were almost missing an entire 100 days from the middle of the observation period. Additionally, each channel showed a noticeable downward trend. Due to the fact that there were two peaks in the CCPD, with neither one having a majority of the correlations contained within the peak, a time lag is indiscernible.

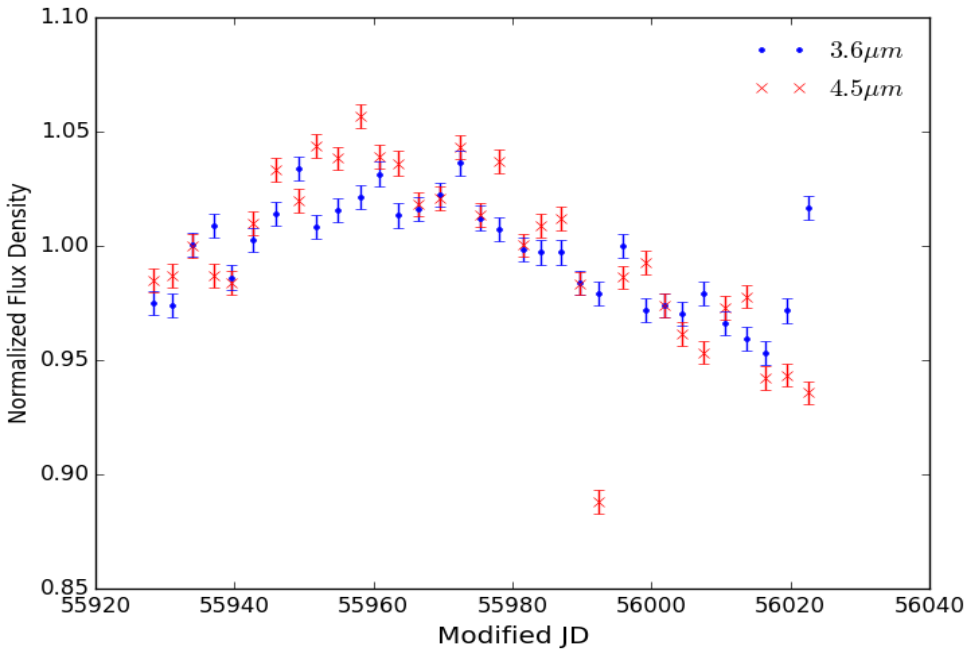

(a)

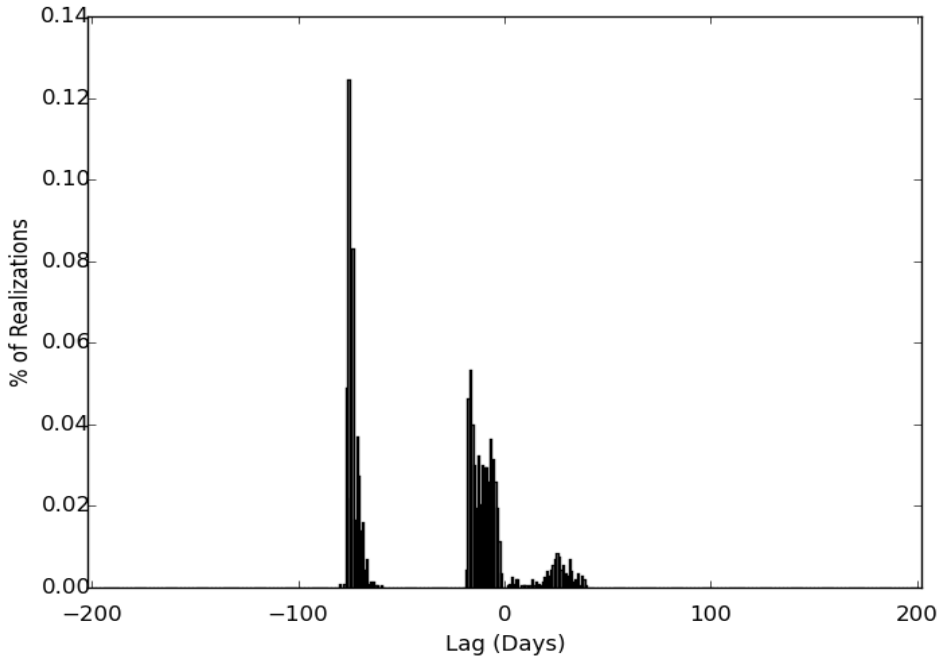

(b)

Figure 5.8: (a) The light curve of MRK 885. (b) The CCPD of MRK885.

5.9 NGC 6418

The Seyfert 1 AGN NGC 6418 both lacks a strong UV continuum and a UV nucleus. In addition to this, the Hα line is the only significant emission source in the spectrum of NGC 6418. These two pieces of information show that the AGN is probably heavily obscured by dust, but because it is a Seyfert 1 galaxy, the dust is not only from the dusty torus (Remillard et al., 1993). There is most likely intervening dust that is contributing to foreground extinction of the emissions.

Because there were multiple gaps in the light curve of NGC 6418, the data before MJD 55928 were ignored for the purposes of the cross correlation. The data for channel 1 had an SNR of 28 while channel 2 had an SNR of 25. NGC 6418's CCPD shows a clearly peaked distribution at a median of -12.3 days. The negative time lag is expected, because channel 2 emissions are expected to lag behind channel 1 emissions. The CCPD shows a single peak; all but six of the correlations were contained within the peak. As expected, the distribution is non-gaussian. These results agree very well with the results found in Vazquez et al. (2015), which concluded that the time lag between the dust emitting at 3.6 μm and 4.5 μm was $13.9^{+0.5}_{-0.1}$ days.

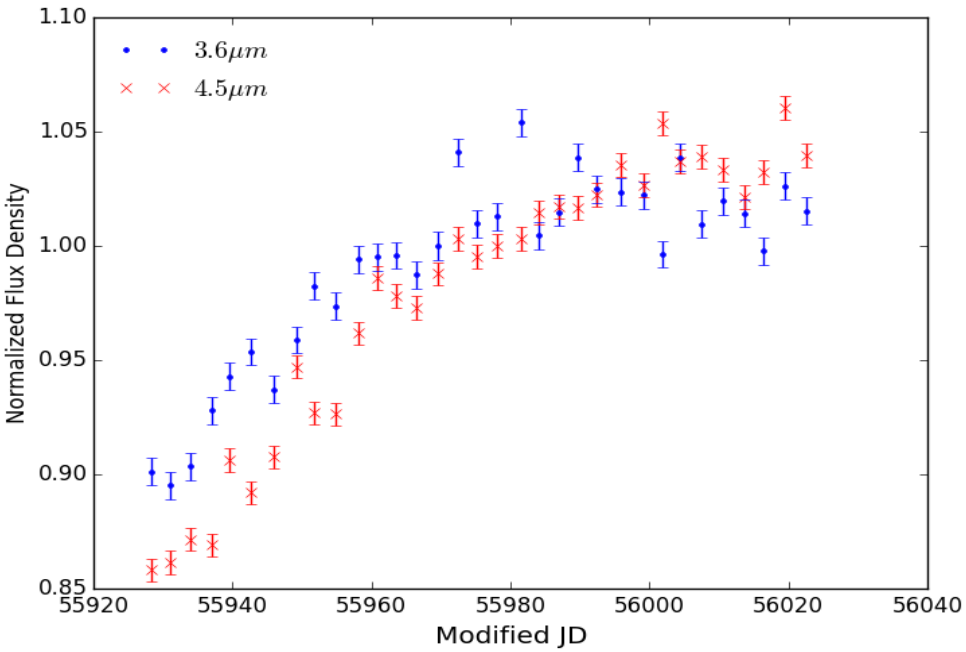

(a)

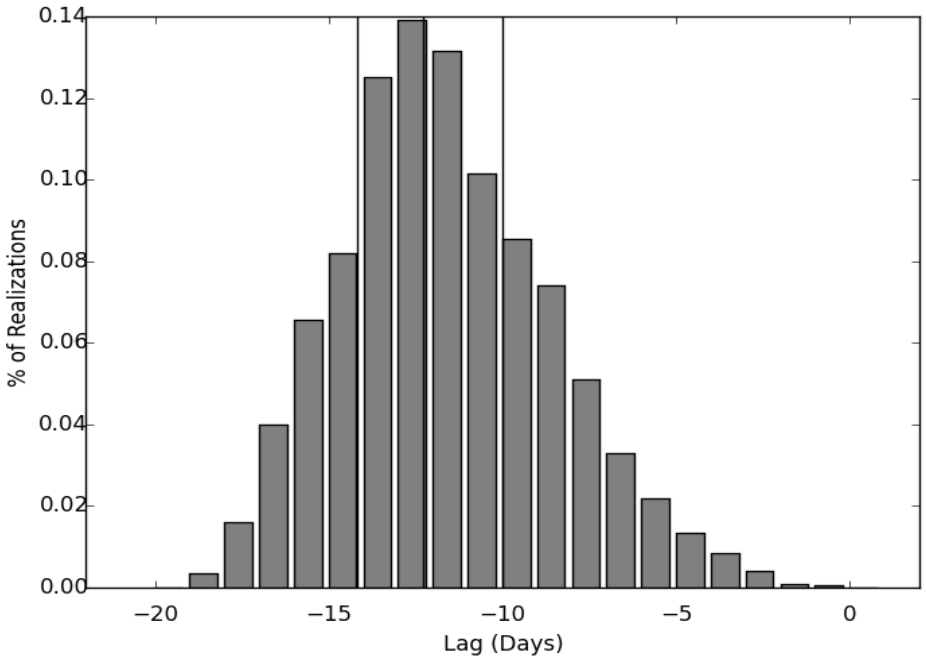

(b)

Figure 5.9: (a) The light curve of NGC 6418. (b) The CCPD of NGC 6418.

5.10 PGC 61965

PGC 61965 is a Seyfert 1 type galaxy that was found to be incredibly variable. The intense variability actually led to PGC 61965 being classified as a BL Lacerte object (Wild, 1975). But after spectroscopic observations, emission lines associated with Seyfert 1 galaxies were found, including a broad H-β line, and so the classification was changed (Wills and Wills, 1979). PGC 61965, under the designation Q 1831+731, was used to help map the High-Velocity Clouds found in the halo of the Milky Way. A high-velocity cloud is a massive cloud that has a velocity that is much higher than it should, for where it is located in the galaxy (Collins et al., 2009).

The FR/RSS algorithm utilized only the light curve data starting on MJD 55928, due to the gaps in the data prior to that MJD. The primary peak in the CCPD, shown in Figure 5.10(b), contained 83% of the total correlations. The primary peak is found at -15.1 days. The lag is not well defined, due to large interquartile range. The distribution for the peak is interesting, because it does not follow the expected distribution for the CCPD. The light curves had the highest measured SNRs, with channel 1 having 177 and channel 2 having 178.

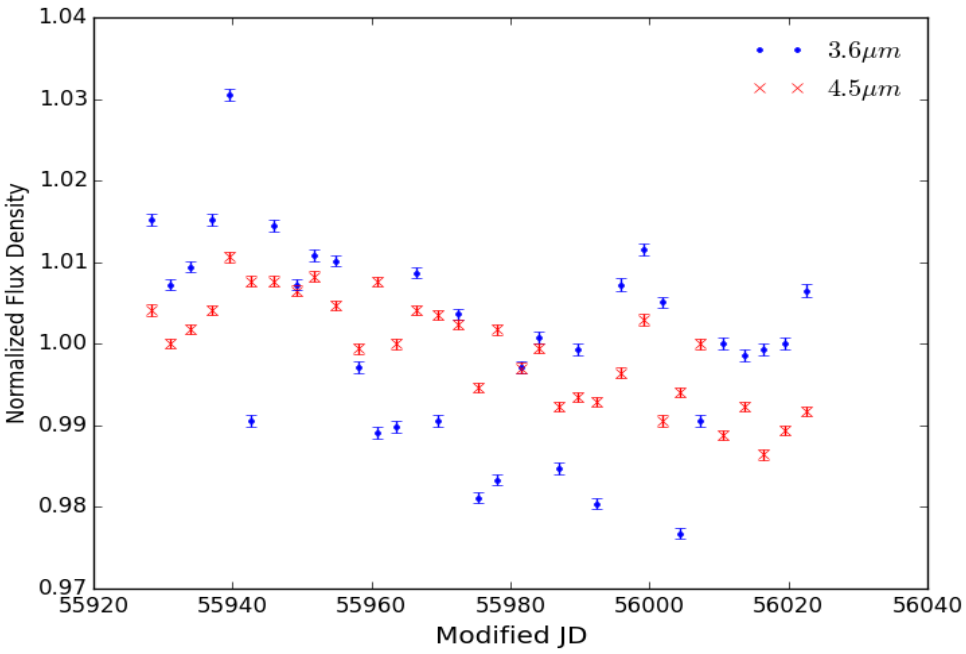

(a)

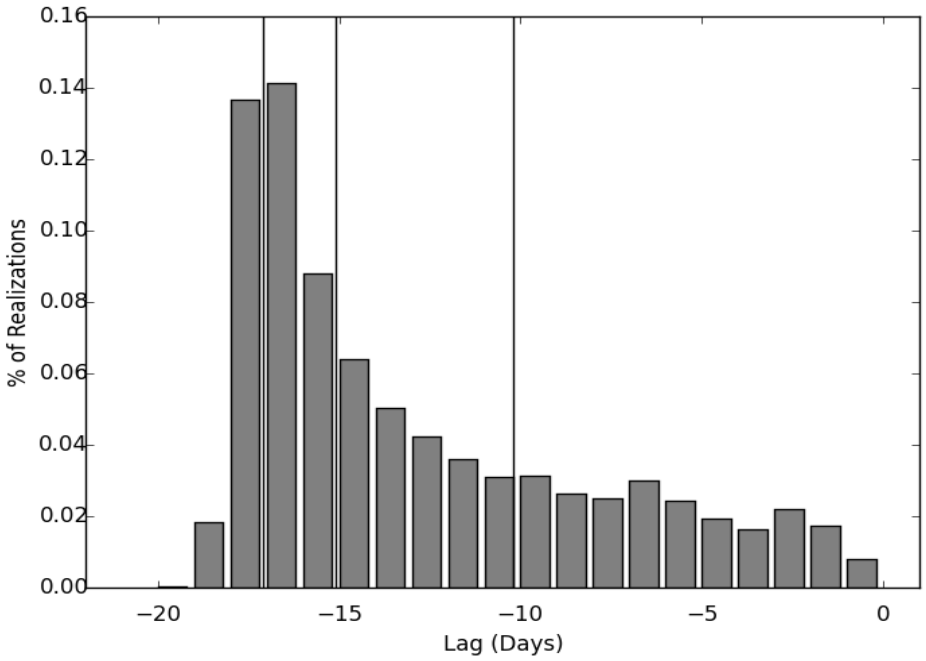

(b)

Figure 5.10: (a) The light curve of PGC 61965. (b) The CCPD of PGC 61965.

5.11 RXSJ 19091+6652

RXSJ 19091+6652 is the second of the two Narrow Line Seyfert 1 AGNs covered in this thesis. At z=0.191, RXSJ 19091+6652 is the farthest target of this thesis. RXSJ 19091+6652 was measured to have a FWHM of 3830.0 km s^{-1}, found in the BLR (specifically in the Hβ line). Additionally, RXSJ 19091+6652 was one of 110 X-ray AGN that were used to model the theory that the BLR comes from outflows (called winds) from the central accretion disk (Xu and Cao, 2007). They found a strong correlation between the accretion rate of the SMBH and the FWHM of the BLR emissions.

The cross correlations for RXSJ 19091+6652 only used observations starting on MJD 55882, as evidenced by the light curves in Figure 5.11(a). Additionally, it had one of the largest SNRs for both channels, with 117 for channel 1 and 118 for channel 2. The CCPD was interesting in note. 89.8% of the cross correlations were found in the peak in Figure 5.11(b), while 9.1% were found in a peak near -110 days. The main peak was found at -26 days. It does not have the expected distribution for normal CCPD peaks, which are expected to be similar to a gaussian distribution. Instead, this behaves more as as exponential due to its heavy, positive side tail. The minimal peak found at -110 days had a similar behavior to the peak shown in Figure 5.11(b).

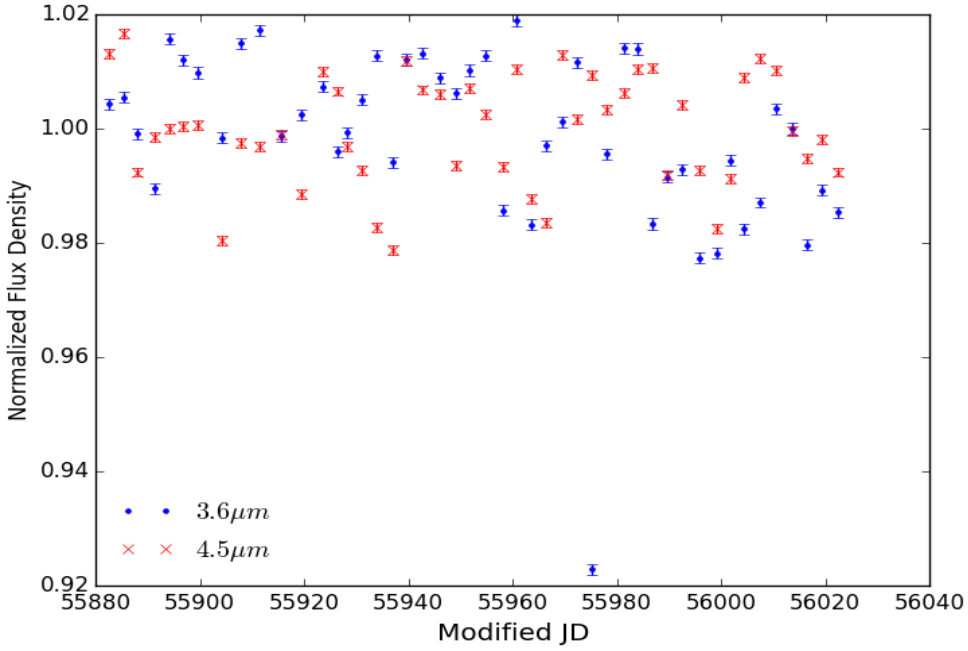

(a)

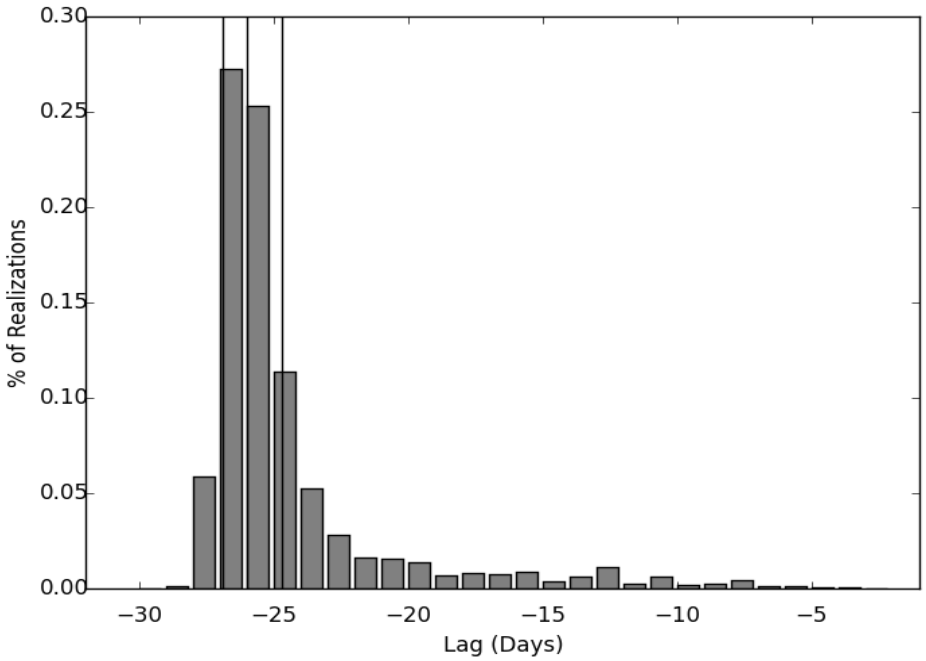

(b)

Figure 5.11: (a)The light curve of RXSJ 19091+6652. (b) The CCPD of RXSJ 19091+6652.

5.12 UGC 10697

UGC 10697 is a typical Seyfert 1 galaxy that has a relatively low redshift (z = 0.053), which means that the galaxy is one of the closer galaxies that were observed. Additionally, the BLR for UGC 10697 has been measured to have a doppler broadening of $\sim$ 3000km s^{-1} (Bade et al., 1995).

The cross correlations were performed on the data following MJD 55882, due to the gaps in the data previous to MJD 55882. UGC 10697 was one of the few AGN that was expected to have the at least one gap in the light curve. The SNR for channel 1 was found to be 131 and the SNR for channel 2 was found to be 114. There is no discernible lag, because no one peak has a distinct majority of the cross correlation realizations. The lack of a lag is fairly well evident in the light curves, as both curves behave very differently throughout the observation period.

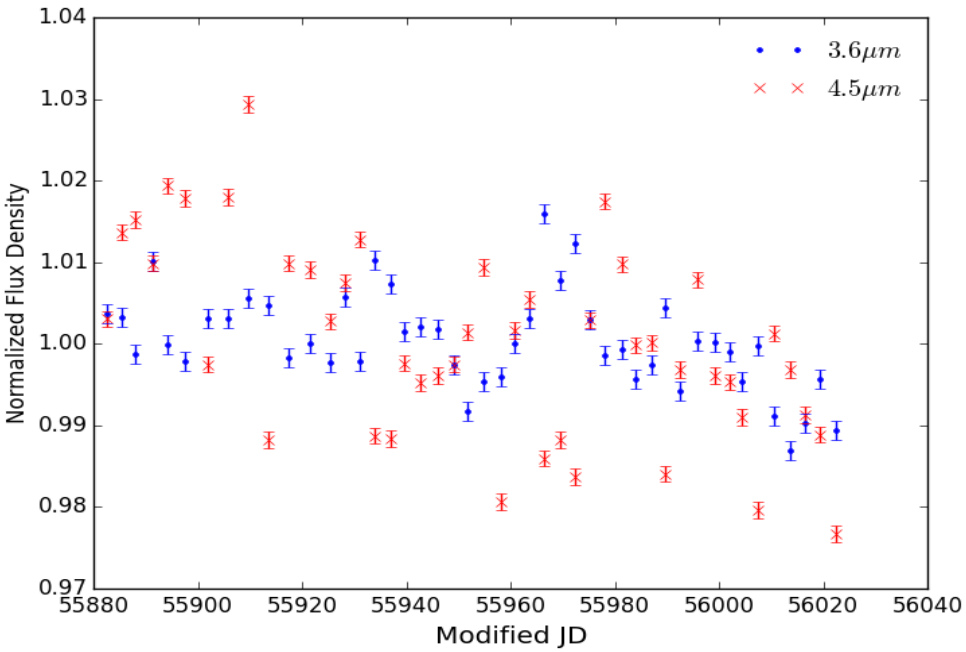

(a)

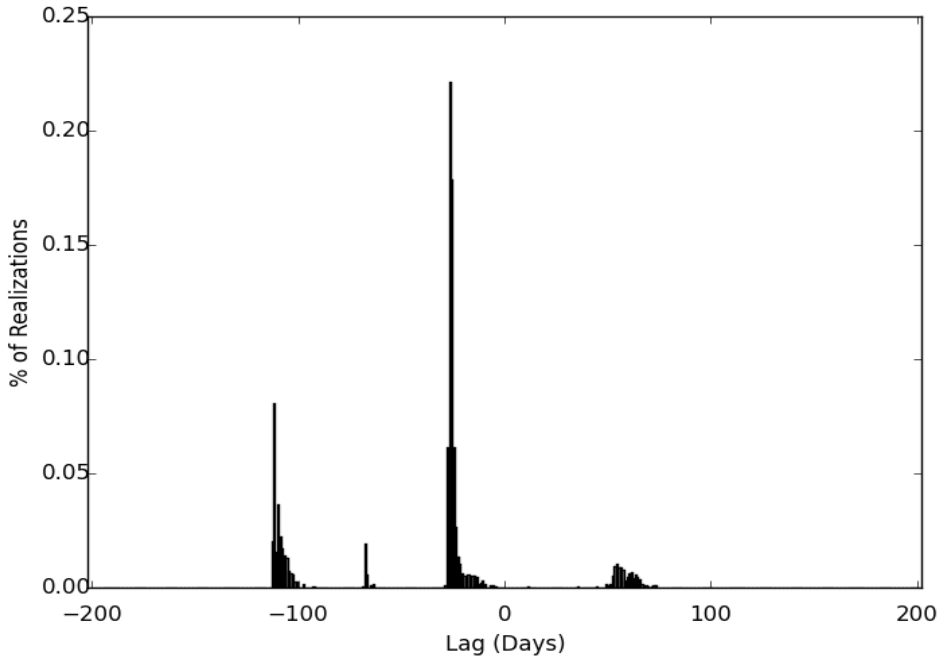

(b)

Figure 5.12: (a) The light curve of UGC 10697. (b) The CCPD of UGC 10697.

Table 5.1: Targets with associated time lag between channels 1 and 2. All lags quoted here are quoted in reference to channel 1 leading channel 2.

Target	Time Lag (Days)
3C 390.3	No discernible lag
AKN524	No discernible lag
IRAS17552+6209	No discernible lag
KAZ102	No discernible lag
KAZ163	No discernible lag
MRK507	No discernible lag
MRK876	No discernible lag
MRK885	No discernible lag
NGC6418	$12.3^{+2.3}_{-1.9}$
PGC61965	$15.1^{+4.9}_{-2.0}$
RXSJ19091+6652	$26.0^{+1.3}_{-0.9}$
UGC10697	No discernible lag

Chapter 6

Discussion

Of the 12 AGN that were studied by this thesis, only NGC 6418 showed a distinct lag between the two channels. The other two AGN that had some sort of a lag recovered were PGC 61965 and RXSJ 19091+6652, but as will be discussed, these were potentially not a real time lag between the channels.

The distribution for NGC 6418 was similar to a gaussian distribution, except that it had a positive skewness and a negative excess kurtosis, which is expected. The extended tail is usually indicative of a CCPD that was constructed from original light curves that didn't have many data points (Peterson et al., 1998). In this case, that probably does not fully explain the tail, because NGC 6418 had 33 data points in the portion, that was used, of the light curve. One possible explanation for the tail being there is that the there is not a distinct cut-off between the clouds that emit in the 3.6 μm and in 4.5μm wavelengths. If the DT was composed of numerous clouds, each individual cloud would emit over multiple wavelengths. This mixing of wavelengths could yield results where the smaller time lag wings in the CCPD would be preferentially favored over the

larger wings. The reason for this favoring comes from how a black body radiates energy; over the wavelengths that a black body will radiate energy, there is a sharp peak in intensity at a specific wavelength (which is only dependent on the temperature of the black body), which tapers off into an extended wing for wavelengths longer than the peak wavelength. What this means for the DT, is that parts of the clouds that emit both wavelengths could be closer to the AGN than the clouds that don't have 3.6 μm emissions, which would make the cross correlation recover shorter time lags.

Both of the remaining AGN that exhibited lag, PGC 61965 and RXSJ 19091+6652, had remarkably different results. Both had more exponential-like correlation distributions, which do not agree with what results are expected from building a distribution of cross correlations. This is most apparent in PGC 61965. The median, which is used to determine the lag, for PGC 61965 does not coincide with the main peak in the distribution, which makes it suspect. Within a CCPD, the tail is not at all expected to be heavy enough to skew the median. Another potential explanation for the tail, assuming its a real result and not a mathematical artifact, could arise from the dust clouds themselves. Smaller than anticipated cloud sizes would affect the cross correlation, for instance, although it would have the effect of recovering potentially longer lags (albeit not by significant amounts). But, this would actually potentially limit the size of the tail, as making the clouds smaller would make the variance in inter-cloud distances smaller as well. Smaller variances would make the spread in the median and interquartile range of the peak, which are the actual measurements used to determine the lag and associated error, smaller. The light curve for PGC 61965 was not very stable, with large fluctuations present,

especially in the 3.6 μm emissions. This instability is probably the cause for the CCPD; cross correlations need a measure of similarity between the two signals.

RXSJ 19091+6652 is different in regards to PGC 61965. The tail, while extended, does not contain a majority (41%) of the correlations that are within the interquartile range of the peak. This means that the median is relatively well found in the main peak. Additionally, at lags that are within $\pm$ 5 days of the median the correlation distribution behaves more like NGC 6418 than PGC 61965. This leads to the possibility that RXSJ 19091+6652 has an actual time lag. The extended tail could be a more extreme case of the potential wavelength mixing as previously described, but most likely it is due to some computational artifacts. RXSJ 19091+6652 also suffers from large variances in the light curves. RXSJ 19091+6652 is a good candidate for further observations, but it doesn't show conclusive enough evidence to warrant further discussion.

The orientation of the DT can also be a factor in the shape of the CCPD. For Seyfert 1 AGN, the DT is assumed to be very near to a face-on orientation, therefore the DT will react at the same time and yield a strong peak in the CCPD at the light crossing time. But, as the inclination is changed, the front edge of the DT will react before the back edge, yielding a "blurring out" of the CCPD, making it broader and less defined (Maoz and Netzer, 1989). The CCPD would still peak at the same τ, as though it were not inclined, due to the fact that the two points perpendicular to the plane on inclination (assuming a simple inclination in only one direction) would not change with respect to the line of sight of observers, but the inclination would yield a foreshortening of the DT; The DT obscures the portion of itself that is closer to the observer. The CCPD would end up being a broader CCPD with a skewness towards the longer

time lag (the longer time lag wing would be more pronounced than the shorter time lag wing).

How the DT responds also contributes to the shape of the CCPD. If the DT was a ring, then the lag would peak solidly at some τ. However, the DT is not a ring; there is a thickness to it. This thickness will also contribute to the lag by broadening the peak as well. A continuum pulse will take time to propagate through the DT, once it has started to interacted with the torus. For a time lag τ and thickness d, the peak would shift to be within the time τ and $\tau + \alpha d$, where α is some constant that describes how long it takes the pulse to traverse a distance in the torus. The peak shouldn't be foreshortened or lengthened, so the wings wouldn't be as effected, except that the longer lag wing would also be shifted away from where it would be for a ring.

Every target that did not show signs of lag had a CCPD that had multiple significant peaks that were separated by large amounts of days. They also usually had peaks in the negative time lags and positive time lags. The multiple peaks have a couple different possible explanations. The first is that the light curves were not similar enough to be able to extract a meaningful time lag from them. Any time a correlation is run on a data set, there will be a correlation coefficient $r = [-1, 1]$ returned. Ideally, completely uncorrelated data will result in a correlation of r = 0. But, in most applications, uncorrelated data returns a non-zero result. For a cross correlation, even if the complete data set is uncorrelated, the algorithm will still a non-zero peak at some time lag, which translates into a peak in the CCPD at some time lag. So, even dissimilar light curves will still have a CCPD built up.

A second possible explanation for the multiple peaks stems from computa-

tional artifacts introduced by the FR/RSS method. By generating artificial light curves from a random subset of the original light curves (in addition to altering each observation by adding a gaussian deviate with a mean of 0 and a standard deviation of the quoted error for each observation), certain points will missing from the generated light curves. If these missing points are important in the correlation (they show a change that is tracked later in the cross correlation), then the actual correlation result will be skewed. If they are unimportant to the actual correlation (i.e. a constant value), then the cross correlation shouldn't be skewed. Additionally, the linear interpolation smooths out missing data points, which can introduce aberrant cross correlations.

Interestingly, almost all of the AGN that did not exhibit a singular defined peak showed some realizations that returned a high negative time lag. A similar effect is seen in a majority of AGN at the opposite end of the time lag spectrum as well. This phenomenon is expected, due to the fact that cross-correlation tends to have end behavior that is inaccurate at best. This is evidenced in Figure 4.2(a), where the both the high positive and negative phase difference (which is analogous to positive and negative time lag) are not symmetrical with each other nor do they exhibit the same sinusoidal signal as the rest of the cross-correlation. This is directly from the fact that, at high positive and negative lags, there are significantly fewer data points that are being correlated. From Equation 4.1, at any time lag τ, there will be $N - \tau$ pairs of data points in the cross correlation. So, for $N = 100$ and $\tau = 95$ days, only 5 data points from each light curve will be used (the first 5 data points of curve x and the last 5 points of curve y). With so few data points, the correlation is very inaccurate.

There are other effects that would propagate through the realizations and

could potentially be found to be the maximum in any given correlation. One such effect would be the sampling rate for the observations. The sampling rate was once every 3 days. Additionally, there was interpolation done in order to bring the sampling to once per day. With this, in some of the correlations, the highest correlation value could fall around -1 to -3 days (the negative due to the fact that channel 2 was correlated with channel 1, which reverses the sign). This is seen in many of the AGN CCPDs. Another effect would be due to the noise in the signal. Noise will introduce random fluctuations that, when correlated, can produce spurious correlations.

Unfortunately, the reverberation mapping technique requires observations of the target's continuum well in advance for mapping the DT. Using the pure graphite model of the inner edge of the torus, the continuum has to be observed more than a year and a half prior to the the DT observation, in order to be able to sample the response of the the DT to the continuum change, for an AGN that has a L_{bol} of 10^{46} erg s^{-1}. If the continuum is not observed, then no information on the distance between the DT and the central source can be determined, although estimates can be made. Such is the case for this thesis project. During the Spitzer observations, which lasted a year, observations of the continuum were not able to be made. Another problem with the technique is that it requires high temporal resolution in observations in order to be able to make a high spatial resolution mapping of the interior structures. This particular project was the first of its kind for high cadence temporal resolution of the DT, so hopefully it will be able to be used as a good base line for similar projects.

Impacting the quality of the data is the fact that telescope downtime was found to occur during the observing program. In the original program, 6 of

the objects (AKN 524, IRAS 17552+6209, KAZ 102, KAZ 163, MRK 507, and NGC 6418) were supposed to be continuously visible throughout the year, with other objects being visible for a large majority of the year. But, on days around MJD 55800 and 55875, the telescope was not observing the targets. Other days were missing on the targets, but that was to be expected.

Even without continuum data, the results from the cross correlation between the two channels can be used. Table 6.1 shows NGC 6418 with its sublimation radii. Because NGC 6418 had only the two channels correlated against each other, the measured time lag will be smaller than the time associated with a photon to cross NGC 6418's graphite sublimation radius, according to the clumpy torus model. In light of the fact that the channels were not correlated with the continuum, the assumption that there is a non-zero time lag between the continuum and both channels will be made in order to analyze the results. The $R_{d,C}$, for NGC 6418, is at least about 50 light days across, which is larger than what K-band ($\sim$ 2.2 μm) measurements have returned for many AGN (Nenkova et al., 2008b; Suganuma et al., 2006). This is probably because larger grains of graphite will survive sublimation at radii that are closer than $R_{d,C}$ (Nenkova et al., 2008b). It must be noted that L_{bol} was estimated for NGC 6418. The average Sy 1 AGN has an $L_{optical}$ that is about 12.2% of the L_{bol} (Risaliti and Elvis, 2004, Chapter 6). Thus, the relation $L_{bol} \approx \frac{L_{optical}}{0.122}$ was used.

The infrared time lag can be roughly estimated from Suganuma et al. (2006)'s fit

$$\tau_K = 0.47 \left(\frac{6\ L_{optical}}{10^{46}\ \text{erg s}^{-1}} \right)^{0.5}\ \text{pc.}$$

This time lag would be the rough lag associated with the K-band, so the es-

timated lag serves as a lower limit for the 3.6 μm time lags. The estimated K-band lag for NGC 6418 would be 40 days. This is roughly consistent with Vazquez et al. (2015). They found that the actual time lag for the 3.6 μm and 4.5 μm emissions were $37.2^{+2.4}_{-2.2}$ and 47.1 ± 3.1 days, respectively.

As per the models mentioned in Axon et al. (2011), if the DT was composed of a solid layer of clouds, then the lag between channels should be about the same as the lag for the 3.6 μm channel. The estimated results and the results from Vazquez et al. (2015) clearly show that the inter-channel lag is decidedly less than the lag time between the continuum and the 3.6 μm emission. This leads credence to the theory that the DT is composed of discrete clouds of dust. Recent observations of the Seyfert 2 AGN NGC 1068 were the first to image the emission from the DT (Garcia-Burillo et al., 2016). Their findings also match models for a clumpy torus.

Table 6.1: NGC 6418's measured time lag, with its associated dust sublimation radii. The sublimation radii has been calculated from Equations 2.4 and 2.5 using L_{bol} estimated from $L_{optical}$ in Table 3.1.

Target	Time Lag (Days)	L_{bol} (erg s^{-1})	$R_{d,C}$ (ld)	$R_{d,Si}$ (ld)
NGC 6418	$12.3^{+2.3}_{-1.9}$	7.09 x 10^{43}	50	130

Chapter 7

Conclusion

The Dusty Torus is a complicated structure, found within AGN, that has only recently started to be explored by astrophysicists. The limited results of this project indicate that only NGC 6418 had a recoverable time lag at $12.3^{+2.3}_{-1.9}$. These results, and estimates made from observable data, seem to indicate that the DT is composed of discrete clouds of dust, which corroborate the results found by Vazquez et al. (2015). While the data allowed for some probing into structure, more work needs to be done in order to have a better understanding of the DT. First, optical and infrared observations need to be done on the AGN. The optical observations allow for more detailed analysis of the structure to be performed, instead of relying on estimates that are only going to be lower limits. Second, as the results from this thesis show, the only AGN that had an interchannel time lag associated with it was NGC 6418, a Sy 1 type galaxy. Knowing this, further observations should be limited to Sy 1 and low intermediate (Sy 1.2) type galaxies until more lags have been measured.

In addition to NGC 6418 showing definitive lag, RXSJ 19091+6652 showed

potential for having a measurable interchannel time lag, at $26^{+1.3}_{-0.9}$. Further observations should be done on RXSJ 19091+6652, in order to determine if the potential lag was spurious or a legitimate signal. Both NGC 6418 and RXSJ 19091+6652 would be good candidates for further studies because they both showed an interchannel lag time of sub-1 month, which is relatively small and thus easily observable in observation programs. At a cadence rate of 3 days per observation (the rate used in this project), that equates to a minimum of 10 observations per target.

Bibliography

Antonucci, R. (1993). Unified Models For Active Galactic Nuclei and Quasars. *Annual Review of Astronomy and Astrophysics*, 31:473–521.

Antonucci, R. R. J. and Miller, J. S. (1985). Spectropolarimetry and the Nature of NGC 1068. *Astrophysical Journal*, 297:621–632.

Astropy Collaboration et al. (2013). Astropy: A community Python package for astronomy. *Astronomy and Astrophysics*, 558:A33.

Axon, D. et al. (2011). Reverberation Mapping of the size of the Dusty Tori in Active Galactic Nuclei. Spitzer Proposal.

Bade, N. et al. (1995). AGN from the ROSAT all-sky survey. *Astronomy and Astrophysics Supplement*, 110:469.

Blandford, R. D. and McKee, C. F. (1982). Reverberation mapping of the emission line regions of Seyfert galaxies and quasars. *Astrophysical Journal*, 255:419–439.

Bock, J. J. et al. (2000). High Spatial Resolution Imaging of NGC 1068 in the Mid-Infrared. *The Astronomical Journal*, 120:2904–2919.

Boyle, B. J. et al. (2002). The 2dF QSO Redshift Survey. In Metcalfe, N. and Shanks, T., editors, *A New Era in Cosmology*, volume 283 of *Astronomical Society of the Pacific Conference Series*, page 72.

California Institute of Technology (2010). IRAC Warm Image Features and Caveats. `http://irsa.ipac.caltech.edu/data/SPITZER/docs/irac/warmfeatures/`.

Carey, S. J. et al. (2010). Properties of Warm IRAC Data. In *American Astronomical Society Meeting Abstracts # 215*, volume 42 of *Bulletin of the American Astronomical Society*, page #481.07.

Collins, J. A., Shull, J. M., and Giroux, M. L. (2009). Hubble Space Telescope Survey of Interstellar High-velocity Si III. *Astrophysical Journal*, 705:962–977.

Dietrich, M. et al. (2012). Optical Monitoring of the Broad-line Radio Galaxy 3C 390.3. *Astrophysical Journal*, 757:53.

Fanaroff, B. L. and Riley, J. M. (1974). The Morphology of Extragalactic Radio Sources of High and Low Luminosity. *Monthly Notices of the Royal Astronomical Society*, 167:31P–36P.

Fazio, G. G. et al. (2004). The Infrared Array Camera (IRAC) for the Spitzer Space Telescope. *Astrophysical Journal Supplement Series*, 154:10–17.

Fowler, A. M. and Gatley, I. (1990). Demonstration of an algorithm for read-noise reduction in infrared arrays. *Astrophysical Journal Letters*, 353:L33.

Fruchter, A. S. and Hook, R. N. (2002). Drizzle: A Method for the Linear Reconstruction of Undersampled Images. *The Publications of the Astronomical Society of the Pacific*, 114:144–152.

Garcia-Burillo, S. et al. (2016). ALMA resolves the torus of NGC 1068: continuum and molecular line emission. *ArXiv e-prints*.

Greenstein, J. L. and Schmidt, M. (1964). The Quasi-Stellar Radio Sources 3c 48 and 3c 273. *Astrophysical Journal*, 140:1.

Halpern, J. P. and Oke, J. B. (1987). Narrow-line Seyfert galaxies with permitted Fe II emission Markarian 507, 5C 3.100, and I ZW 1. *Astrophysical Journal*, 312:91–100.

Hutchings, J. B. and Hickson, P. (1988). Extended emission-line regions in active galaxies. *The Astronomical Journal*, 95:1363–1370.

Hutchings, J. B. and Neff, S. G. (1992). Optical imaging of QSOs with 0.5 arcsec resolution. *The Astronomical Journal*, 104:1–14.

IBM Corporation (2013). *IBM SPSS Statistics for Windows, Version 22.0*. IBM Corporation, Armonk, NY.

IRAC Instrument and Instrument Support Teams (2012). *IRAC Instrument Manual*. Version 2.0.2.

Jansky, K. G. (1932). Directional Studies of Atmospherics at High Frequencies. In Kassim, N., Perez, M., Junor, W., and Henning, P., editors, *From Clark Lake to the Long Wavelength Array: Bill Erickson's Radio Science*, volume 345 of *Astronomical Society of the Pacific Conference Series*, pages 3–15.

Jansky, K. G. (1933). Electrical phenomena that apparently are of interstellar origin. *Popular Astronomy*, 41:548.

Jansky, K. G. (1935). A Note on the Source of Interstellar Interference. *Proceedings of the Institute of Radio Engineers*, 23(10):1158–1163.

Jiménez-Benito, L., Díaz, A. I., Terlevich, R., and Terlevich, E. (2000). Stellar indices and kinematics in Seyfert 1 nuclei. *Monthly Notices of the Royal Astronomical Society*, 317:907–921.

Kazanas, D., Fukumura, K., Behar, E., Contopoulos, I., and Shrader, C. (2012). Toward a Unified AGN Structure. *The Astronomical Review*, 7(3):030000–123.

Komossa, S. (2008). Narrow-line Seyfert 1 Galaxies. In *Revista Mexicana de Astronomia y Astrofisica Conference Series*, volume 32 of *Revista Mexicana de Astronomia y Astrofisica Conference Series*, pages 86–92.

Koratkar, A. and Blaes, O. (1999). The Ultraviolet and Optical Continuum Emission in Active Galactic Nuclei: The Status of Accretion Disks. *The Publications of the Astronomical Society of the Pacific*, 111:1–30.

Kriss, G. A. and Canizares, C. R. (1982). Optical and X-ray properties of X-ray selected active galactic nuclei. *Astrophysical Journal*, 261:51–63.

Lynden-Bell, D. (1969). Galactic Nuclei as Collapsed Old Quasars. *Nature*, 223:690–694.

Lynds, R. (1971). The Absorption-Line Spectrum of 4c 05.34. *Astrophysical Journal Letters*, 164:L73.

Makovoz, D. and Khan, I. (2005). Mosaicking with MOPEX. In Shopbell, P., Britton, M., and Ebert, R., editors, *Astronomical Data Analysis Software and Systems XIV*, volume 347 of *Astronomical Society of the Pacific Conference Series*, page 81.

Maoz, D. and Netzer, H. (1989). Evaluation of the cross-correlation method and the size of AGN emission-line regions. *Monthly Notices of the Royal Astronomical Society*, 236:21–29.

Mor, R. and Netzer, H. (2012). Hot graphite dust and the infrared spectral energy distribution of active galactic nuclei. *Monthly Notices of the Royal Astronomical Society*, 420:526–541.

Nenkova, M., Sirocky, M. M., Ivezić, Ž., and Elitzur, M. (2008a). AGN Dusty Tori. I. Handling of Clumpy Media. *Astrophysical Journal*, 685:147–159.

Nenkova, M., Sirocky, M. M., Nikutta, R., Ivezić, Ž., and Elitzur, M. (2008b). AGN Dusty Tori. II. Observational Implications of Clumpiness. *Astrophysical Journal*, 685:160–180.

Nikutta, R., Elitzur, M., and Lacy, M. (2009). On the 10 μm Silicate Feature in Active Galactic Nuclei. *Astrophysical Journal*, 707:1550–1559.

Osterbrock, D. E. (1981). Seyfert galaxies with weak broad H alpha emission lines. *Astrophysical Journal*, 249:462–470.

Penston, M. V. and Perez, E. (1984). An evolutionary link between Seyfert I and II galaxies? *Monthly Notices of the Royal Astronomical Society*, 211:33P–39P.

Peterson, B. M. (2001). Variability of Active Galactic Nuclei. In Aretxaga, I., Kunth, D., and Mújica, R., editors, *Advanced Lectures on the Starburst-AGN*, page 3.

Peterson, B. M. et al. (1998). On uncertainties in cross-correlation lags and the reality of wavelength-dependent continuum lags in active galactic nuclei. *Publications of the Astronomical Society of the Pacific*, 110(748):pp. 660–670.

Peterson, B. M. and Horne, K. (2004). Echo mapping of active galactic nuclei. *Astronomische Nachrichten*, 325:248–251.

Press, W. H., Teukolsky, S. A., Vetterling, W. T., and Flannery, B. P. (2007). *Numerical Recipes 3rd Edition: The Art of Scientific Computing*. Cambridge University Press, 3 edition.

Raban, D., Jaffe, W., Röttgering, H., Meisenheimer, K., and Tristram, K. R. W. (2009). Resolving the obscuring torus in NGC 1068 with the power of infrared interferometry: revealing the inner funnel of dust. *Monthly Notices of the Royal Astronomical Society*, 394:1325–1337.

Rees, M. J. (1966). Appearance of Relativistically Expanding Radio Sources. *Nature*, 211:468–470.

Remillard, R. A. et al. (1993). Twenty-two emission-line AGNs from the HEAO-1 X-ray survey. *The Astronomical Journal*, 105:2079–2089.

Risaliti, G. and Elvis, M. (2004). A Panchromatic View of AGN. In Barger, A. J., editor, *Supermassive Black Holes in the Distant Universe*, volume 308 of *Astrophysics and Space Science Library*, page 187.

Rodriguez-Pascual, P. M., Mas-Hesse, J. M., and Santos-Lleo, M. (1997). The broad line region of narrow-line Seyfert 1 galaxies. *Astronomy and Astrophysics*, 327:72–80.

Salpeter, E. E. (1964). Accretion of Interstellar Matter by Massive Objects. *Astrophysical Journal*, 140:796–800.

Sandage, A. (1965). The Existence of a Major New Constituent of the Universe: the Quasistellar Galaxies. *Astrophysical Journal*, 141:1560.

Seyfert, C. K. (1943). Nuclear Emission in Spiral Nebulae. *Astrophysical Journal*, 97:28.

Slipher, V. M. (1917). The spectrum and velocity of the nebula N.G.C. 1068 (M 77). *Lowell Observatory Bulletin*, 3:59–62.

Stalevski, M., Fritz, J., Baes, M., and Popovic, L. C. (2013). The AGN dusty torus as a clumpy two-phase medium: radiative transfer modeling with SKIRT. *ArXiv e-prints*.

Suganuma, M. et al. (2006). Reverberation Measurements of the Inner Radius of the Dust Torus in Nearby Seyfert 1 Galaxies. *Astrophysical Journal*, 639:46–63.

Vazquez, B. et al. (2015). Spitzer Space Telescope Measurements of Dust Reverberation Lags in the Seyfert 1 Galaxy NGC 6418. *Astrophysical Journal*, 801:127.

Véron-Cetty, M.-P., Véron, P., and Gonçalves, A. C. (2001). A spectrophotometric atlas of Narrow-Line Seyfert 1 galaxies. *Astronomy and Astrophysics*, 372:730–754.

Werner, M. W. et al. (2004). The Spitzer Space Telescope Mission. *Astrophysical Journal Supplement Series*, 154:1–9.

Wild, P. (1975). Probable Nova in Scutum. *IAU Central Bureau for Astronomical Telegrams*, 2791:1.

Wills, B. J. and Wills, D. (1979). Spectroscopy of 125 QSO candidates and radio galaxies. *Astrophysical Journal Supplement Series*, 41:689–700.

Xanthopoulos, E. and De Robertis, M. M. (1991). Broadband imaging of eight isolated (?) Seyfert galaxies. *The Astronomical Journal*, 102:1980–1990.

Xu, Y. and Cao, X.-W. (2007). Evidence of the Link between Broad Emission Line Regions and Accretion Disks in Active Galactic Nuclei. *Chinese Journal of Astronomy and Astrophysics*, 7:63–70.

Yee, H. K. C. and Green, R. F. (1987). The environment of the quasar PG 1613 + 65 (Mkn 876) - A close interacting pair. *The Astronomical Journal*, 94:618–627.